



## Research paper

# Nodal discontinuous Galerkin spectral formulation for mooring problems with snap loads, including bending and torsion



A.F.L. Governo \*, J.C.C. Henriques , L.M.C. Gato

<sup>a</sup>IDMEC, Instituto Superior Técnico, Universidade de Lisboa, Av. Rovisco Pais 1, 1049-001, Lisboa, Portugal

## ARTICLE INFO

**Keywords:**  
 Moorings  
 Snap loads  
 Discontinuous Galerkin  
 Bending stiffness

## ABSTRACT

High-resolution numerical schemes remain underutilized in mooring line analysis of floating wind turbines and wave energy converters. The need to simulate impulsive dynamics such as snap loads — propagation of abrupt tension variations along the line — also requires shock-capturing methods capable of robustly handling these phenomena across a wide range of mooring materials, configurations, and load conditions. This work presents a nodal discontinuous Galerkin spectral element method for solving the non-linear dynamic equations of submerged mooring lines with high-order accuracy and low-dispersion errors, essential for wave propagation problems. The model accounts for hydrodynamic forces via Morison's equation, includes current loading, seabed contact, and incorporates bending and torsional effects that preserve high-order strain gradients. Comprehensive validation and verification against analytical, numerical, and experimental benchmarks from the literature demonstrates the method's superior accuracy and performance, and its robustness for handling slack cable conditions conducive to snap loading. This capability is particularly critical for offshore renewable energy applications where accurate prediction of these loads is essential to prevent premature failures.

## 1. Introduction

The marine renewable energy industry, including the floating wind and wave energy sectors, faces challenges such as high costs, reliability, and survivability (Rui et al., 2024). Cost reduction is essential for the competitiveness of these sectors, with moorings playing a crucial role due to their impact on CapEx. Mooring systems account for up to 10% of the total structural costs, making their early-stage design critical for projects (Davidson and Ringwood, 2017).

The design of a reliable mooring system requires an iterative approach, with the testing of different line configurations, materials, dimensions and other factors, before converging to an optimal solution (Pecher and Kofoed, 2017). Although costly in time and resources, physical testing is essential for confirming or refuting the anticipated performance of the final design. On the other hand, numerical models are a cost-effective way of simulating mooring configurations under various conditions and parameters, without the high costs and logistical challenges of physical testing. After validation, they can predict the overall response of floating offshore structures and mooring loads with known accuracy, facilitating data-driven decisions before testing (Qiao et al.,

2020). Consequently, developing more sophisticated numerical tools is a valuable approach to enhancing pre-testing analysis capabilities.

Since the early 1960s, the offshore sector, mainly through the oil and gas industry, has stimulated the development of theoretical frameworks and numerical methods related to line/cable analysis and design. Significant work has been conducted in various fields, including mooring, towing, instrumentation deployment, and risers, with multiple admissible approaches depending on the specific application (Chakrabarti, 2005). Quasi-static line models are prevalent in the analysis of offshore oil and gas structures but their utilization in modern offshore floating devices, such as Wave Energy Converters (WECs) and Floating Offshore Wind Turbines (FOWTs), is inadequate due to the dynamically complex and non-linear behaviour of these systems (Nava et al., 2013; Masciola et al., 2012; Brown and Mavrakos, 1999; Masciola et al., 2013; Hall et al., 2014). The most rigorous way for measuring breaking/ultimate and fatigue loads under highly non-linear conditions, such as low-tension regimes, snap loads, and complex seabed interactions, is through advanced dynamic modelling (DNV-GL, 2018). Furthermore, bending effects should be appropriately considered for low-tension and synthetic lines, as they impact fatigue damage, while torsion has

\* Corresponding author.

E-mail addresses: [andre.governo@tecnico.ulisboa.pt](mailto:andre.governo@tecnico.ulisboa.pt) (A.F.L. Governo), [joaochenriques@tecnico.ulisboa.pt](mailto:joaochenriques@tecnico.ulisboa.pt) (J.C.C. Henriques), [\(L.M.C. Gato\).](mailto:luis.gato@tecnico.ulisboa.pt)

<b>Nomenclature</b>	
<i>Romans</i>	
$a$	Acceleration [m/s <sup>2</sup> ]
$A$	Area [m <sup>2</sup> ]
$\hat{\mathbf{b}}$	Unitary binormal vector [-]
$d$	Diameter [m]
$c$	Wave speed [m/s]
$C$	Coefficient [-]
$\ \mathbf{e}\ _{L_2}$	$L_2$ -norm of the absolute error
$\hat{\mathbf{e}}$	Unitary vector [-]
$E$	Young's modulus [Pa]
$\mathbf{f}$	Distributed force vector per unit length [N/m]
$\mathbf{F}$	Numerical fluxes
$\mathbf{F}^*$	Riemann solver
$k_{sb}$	Seabed stiffness [Pa/m]
$L$	Line length [m]
$\ell$	Lagrangian basis functions
$m$	Mass [kg]
$\mathbf{M}$	Internal moment vector [N]
$\hat{\mathbf{n}}$	Unitary normal vector [-]
$\mathbf{r}$	Position vector [m]
$R$	Radius [m]
$s$	Unstretched line coordinate [m]
$\mathbf{S}$	Source terms vector
$t$	Time [s]
$T$	Tensile force magnitude [N]
$\mathbf{T}$	Internal force vector [N]
$\hat{\mathbf{t}}$	Unitary tangential vector [-]
$\mathbf{U}$	Conservative variables vector
$\mathbf{v}$	Absolute velocity [m/s]
$z$	Vertical coordinate [m]
<i>Greek symbols</i>	
$\alpha$	Blending coefficient [-]
$\beta$	Damping coefficient [-]
$\gamma$	Torsion angle [m <sup>-1</sup> ]
$\Delta$	Variation, interval
$\delta_{ij}$	Kronecker delta
$\epsilon$	Indicator quantity [-]
$\varepsilon$	Axial strain [-]
$\xi$	Reference space coordinate [-]
$\kappa$	Curvature [m <sup>-1</sup> ]
$\lambda$	Eigenvalue [m/s]
$\lambda$	Eigenvalues matrix [m/s]
$\mu$	Dynamic friction coefficient [-]
$\rho$	Density [kg/m]
$\tau$	Period [s]
$\omega$	Quadrature weights [-]
<i>Subscripts</i>	
0	Initial conditions / unstretched quantities
A	Added mass
B	Buoyancy
c	Convective
C	Contact
d	Diffusive
D	Drag
max	Maximum
min	Minimum
n	Normal
rel	Relative
sb	Seabed
t	Tangential
w	Water
<i>Acronyms</i>	
CFL	Courant Friedrichs Lewy
DG	Discontinuous Galerkin
DGSEM	Discontinuous Galerkin Spectral Element Method
FOWT	Floating Offshore Wind Turbine
FEM	Finite-Element Method
FVM	Finite-Volume Method
FDM	Finite-Difference Method
LGL	Legendre-Gauss-Lobatto
LM	Lumped-Mass
ODE	Ordinary Differential Equation
PDE	Partial Differential Equation
WEC	Wave Energy Converter

negligible impact in most cases (Hall et al., 2014). Examples include taut systems and remotely operated vehicles maneuvering (Triantafylou and Howell, 1994).

The dynamic behaviour of submerged lines is governed by a system of non-linear partial differential equations for which analytical solutions are impossible without limiting assumptions. Consequently, designers resort to several numerical techniques for solving them, with varying degrees of complexity. In the literature, there are three primary categories of numerical theories relating to mooring line dynamics: Finite-Element Method (FEM) (Aamo and Fossen, 2000; Garrett, 1982; Buckham et al., 2004; Petrone et al., 2016), Finite-Difference Method (FDM) (Ablow and Schechter, 1983; Gobat and Grosenbaugh, 2001; Howell, 1992; Tjavaras, 1996) and Lumped-Mass (LM) models. The LM model can be regarded as a subset of the FEM, as it represents a simplification of the higher-order model. Walton and Polacheck are widely recognized as pioneers in submerged cable numerical modelling, having developed a finite difference spatial discretisation consisting of inextensible cable segments connected by joints (Walton and Polacheck, 1960). The cable is divided into a series of nodes positioned at the centre of the segments, where masses and loads are concentrated, i.e. "lumped", and where the solution is evolved. Their model was later improved to include elasticity, by connecting the nodes with a linear spring (Polacheck et al.,

1963). Howell (1992), Tjavaras (1996), and Gobat (2000) made significant advancements in finite difference methods for cables, building on the work of Ablow and Schechter (1983). Their contributions include the introduction of the generalized- $\alpha$  implicit time discretisation, the box method, and bending and torsional effects modelling (Gobat and Grosenbaugh, 2001). The FEM is probably the most well-established and used formulation in the offshore mooring and riser industry. It consists of a discretisation into elements, where the physical quantities of interest are approximated by basis functions. The accuracy of the discretisation depends on the degree of the basis functions, which can be linear (Aamo and Fossen, 2000; Azconea et al., 2017) or of high-order (cubic or more) (Nordgren, 1974; Garrett, 1982; Buckham et al., 2004; Palm et al., 2017). Other mathematical formulations exist, such as one-dimensional beam models that include elasticity, shear, bending and torsion (Quan et al., 2020; Martin and Bihs, 2021). Anchor dynamics for embedded anchoring are treated in Wang et al. (2020), Rui et al. (2023, 2025).

A perfectly flexible line with no bending or torsion (as is reasonable for chains) results in a hyperbolic system of PDEs, provided the tension is non-negative (Rao, 2011). Waves propagate through the line at a speed proportional to the square root of the tension, serving as the primary mechanism of energy transfer (Cristescu, 2007). Even with smooth initial conditions, solutions to non-linear hyperbolic conservation laws

often exhibit discontinuities (shocks), which pose significant challenges in numerical simulations. In moorings, a snap load propagates through the line as a tension discontinuity or shock. This motivated the use of a finite-element approach, which allows local discontinuous solutions: the so-called Discontinuous Galerkin (DG) methods, first introduced by Reed and Hill (1973). The DG methods approximate the local element-wise solution using polynomials of arbitrary order, and account for the characteristics of wave propagation through Riemann solvers, borrowed from the finite volume methodology (LeVeque, 2002). They are now becoming increasingly popular in both industry and academia because of their efficiency and good numerical properties, namely low dispersion and dissipation errors, making them appropriate to solve hyperbolic and elliptic problems (Karniadakis and Sherwin, 2005). Different versions of this method have been used to a lesser extent in this field. Montano et al. (2007) algorithm considers tension values to be discontinuous, yet maintains continuity in line displacements. Palm et al. (2017) develops a local DG scheme for solving the line non-linear PDE in conservative form, focusing on snap load capture and including bending and torsion effects through-beam models in the momentum balance equation (Palm and Eskilsson, 2020). More recently, Governo et al. (2023) implements a conservative second-order Finite-Volume Method (FVM) with the same capabilities for snap loading regimes. Note that the FVM can be considered a specialized version of the FEM methodology for piecewise constant basis functions.

Robust mooring system analysis for offshore floating devices requires conducting long-term statistical simulations subjected to stochastic environmental loading. Thus, computationally efficient and accurate numerical algorithms are essential. Among the most efficient variants of the DG methods are nodal collocation-type DG schemes, such as the Discontinuous Galerkin Spectral Element Method (DGSEM). In this approach, the solution is approximated using Lagrangian interpolating polynomials, with collocation at the interpolation and quadrature nodal points. This differs from the approach of Palm et al. (2017) that uses orthogonal Legendre polynomials as basis functions; thus, the degrees of freedom represent modal coefficients rather than point values. Both approaches are in fact complementary and are connected through the Vandermonde matrix (Hesthaven and Warburton, 2008). For an overview of the literature in DG methods and their variants, we refer to the books of Karniadakis and Sherwin (2005) for modal polynomial expansions and to Hesthaven and Warburton (2008) for nodal basis functions.

The present study developed a high-order accurate DGSEM for solving the non-linear equations of submerged line dynamics, in conservative form. For enhanced robustness in the presence of shocks, a hybrid DGSEM/FV blending scheme coupled the nodal DG method with a Legendre-Gauss-Lobatto (LGL) finite-volume subcell grid. Additionally, a momentum conservation-based formulation was employed to account for strain gradients in bending and torsion modelling. The numerical framework included a torsional component; however, explicit test cases that demonstrate and validate this were out of scope. The method was tested against various test cases from the literature.

The most relevant contributions can be summarised in the following topics:

- A high-order DGSEM numerical scheme for simulating submerged mooring line dynamics that captures wave propagation and discontinuous snap load events with superior accuracy compared to traditional methods.
- Modelling of bending and torsion effects having into account high-order strain gradients.
- Verification and validation test cases shows the accuracy and convergence properties as well as suitability for simulating complex dynamics.

The paper's structure is as follows. Section 2 presents the governing equations for the line dynamics problem written in the conservative form and the necessary assumptions required for their calculation. Next, in Section 3 the numerical formulation for the system of hyperbolic PDEs

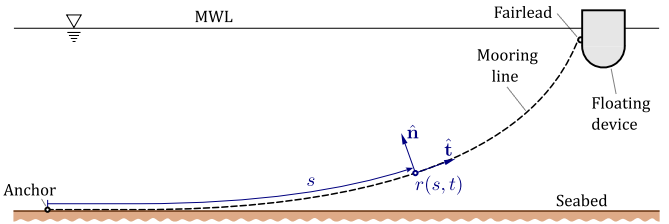


Fig. 1. Coordinate system for the mooring line on an inertial frame of reference, fixed at the anchor point (Governo et al., 2023).

is developed based on the DG spectral element method. Numerical results of the newly developed scheme in selected validation cases are presented in Section 4, while conclusions appear in Section 5.

## 2. Numerical modelling

### 2.1. Governing equations

The equations of motion of a single mooring line can be derived in various coordinate systems. However, in the subsequent analysis, an inertial frame of reference was used (Aamo and Fossen, 2000, 2001). The motion of the mooring line was described by the curvilinear coordinate  $s$ , measured along the length of the line from the origin (anchor point), as shown in Fig. 1.

Here, the anchor point is at the seabed surface; thus, embedded anchor dynamics of suction and drag-embedment anchors are neglected (Xiong et al., 2016).

The three-dimensional line kinematics is uniquely characterized by the motion of its centreline,  $\mathbf{r}(s, t) \in \mathbb{R}^3$ , for  $s \in [0, L_0]$ , where  $s$  denotes the unstretched distance of a certain material point from the origin and  $L_0$  is the unstretched line length (hereforth, the subscript 0 denotes unstretched quantities). At any point in the curve  $\mathbf{r}(s, t)$ , the tension in the mooring is denoted by  $\mathbf{T}(s, t)$ . It is also helpful to define the so-called Frenet-Serret reference frame  $(\hat{\mathbf{t}}, \hat{\mathbf{n}}, \hat{\mathbf{b}})$  local to the material point, defined through

$$\hat{\mathbf{t}} = \frac{\partial \mathbf{r}}{\partial s} \left\| \frac{\partial \mathbf{r}}{\partial s} \right\|^{-1}, \quad (1a)$$

$$\hat{\mathbf{n}} = \frac{\partial \hat{\mathbf{t}}}{\partial s} \left\| \frac{\partial \hat{\mathbf{t}}}{\partial s} \right\|^{-1}, \quad (1b)$$

$$\hat{\mathbf{b}} = \hat{\mathbf{t}} \times \hat{\mathbf{n}}, \quad (1c)$$

where the tangent  $\hat{\mathbf{t}}$ , normal  $\hat{\mathbf{n}}$ , and binormal  $\hat{\mathbf{b}}$  unit vectors form an orthonormal basis. Here,  $\|\cdot\|$  represents the Euclidean norm in  $\mathbb{R}^3$ . Note that the line's shape changes with time; thus, this system of vectors is a function of  $s$ . The curvature vector  $\kappa(s)$  is given by

$$\kappa = \frac{\partial \hat{\mathbf{t}}}{\partial s}. \quad (2)$$

The conservation of linear momentum in a line leads to the following system of equations (Aamo and Fossen, 2000),

$$\frac{\partial}{\partial t} (m_0 \mathbf{v}) = \frac{\partial \mathbf{T}}{\partial s} + \mathbf{f}(1 + \varepsilon), \quad (3)$$

where  $\mathbf{v}(s, t)$  is the velocity vector, and  $\mathbf{f}(s, t)$  is the distributed external forces vector per unit length. The mass of the line per unit of length  $m_0$  is assumed to be constant, and  $\varepsilon$  represents the (axial) strain, calculated with

$$\varepsilon = \left\| \frac{\partial \mathbf{r}}{\partial s} \right\| - 1, \quad (4)$$

which leads to

$$\hat{\mathbf{t}} = \frac{1}{1 + \varepsilon} \frac{\partial \mathbf{r}}{\partial s}. \quad (5)$$

The internal force vector is divided into its axial and bending components,  $\mathbf{T} = \mathbf{T}_t + \mathbf{T}_b$ , respectively. For a line with negligible bending

and torsional stiffness, the bending component is zero (Aamo and Fos-sen, 2001), which is a reasonable assumption for chains and mooring lines in most conditions. The magnitude of the tangential force  $T$  is calculated according to a functional relation of the strain and strain rate,  $T = T(\varepsilon, \partial\varepsilon/\partial t)$ . Under the assumption that Hooke's law applies and compression is not allowed in the material, it is

$$T = EA_0 \max(\varepsilon, 0) + \beta \frac{\partial\varepsilon}{\partial t}. \quad (6)$$

where  $EA_0$  is the line's axial stiffness and  $\beta$  is a damping term proportional to the strain rate. Then, the tangential component of the vector is simply  $\mathbf{T}_t = T\hat{\mathbf{t}}$ . Substituting Eq. (5), the equation becomes

$$m_0 \frac{\partial\mathbf{v}}{\partial t} = \frac{\partial}{\partial s}(T\hat{\mathbf{t}} + \mathbf{T}_b) + \mathbf{f}(1 + \varepsilon). \quad (7)$$

By introducing  $\mathbf{q}(s, t)$  as

$$\mathbf{q} = \frac{\partial\mathbf{r}}{\partial s}, \quad (8)$$

the compatibility relations of continuity and differentiability in the system are expressed through (Governo et al., 2023)

$$\frac{\partial\mathbf{q}}{\partial t} = \frac{\partial\mathbf{v}}{\partial s}. \quad (9)$$

## 2.2. External forces

The external force vector  $\mathbf{f}$  contains the environmental distributed loads per unit length exerted on the line, namely gravity, hydrostatic and hydrodynamic forces. The seabed also exerts a force when the line rests on it. Therefore,

$$\mathbf{f} = \mathbf{f}_B + \mathbf{f}_A + \mathbf{f}_D + \mathbf{f}_C, \quad (10)$$

where  $\mathbf{f}_B$  is the buoyancy and weight force,  $\mathbf{f}_A$  is the added mass and Froude-Krylov force,  $\mathbf{f}_D$  is drag force, and  $\mathbf{f}_C$  is the bottom contact force.

The net result of the weight and buoyancy forces acting at each node can be combined into what is called the submerged weight  $\mathbf{f}_B$  and is given by

$$\mathbf{f}_B = \frac{m_0}{1 + \varepsilon} \left( 1 - \frac{\rho_w}{\rho_c} \right) (-g \hat{\mathbf{e}}_z), \quad (11)$$

where  $\rho_w$  and  $\rho_c$  are the densities of water and line material, respectively,  $g$  is the gravitational acceleration constant and  $\hat{\mathbf{e}}_z$  is the unit vector along the  $z$ -axis.

The hydrodynamic loads exerted on the line are due to the relative motion between the line and the surrounding fluid and are estimated with the well-known Morison's equations (Faltinsen, 1999). The unsteady Froude-Krylov force due to the surrounding pressure field is included in the inertial component. The added mass force is,

$$\mathbf{f}_A = \frac{1}{4} \rho_w \frac{\pi d_0^2}{(1 + \varepsilon)} \left( \mathbf{a}_w + C_{A_t} \mathbf{a}_{rel_t} + C_{A_n} \mathbf{a}_{rel_n} \right), \quad (12)$$

where  $C_{A_t}$  and  $C_{A_n}$  are the non-dimensional coefficients of added mass in the tangential and normal directions, respectively, and  $d_0$  is the unstretched diameter of the line. This force depends on the current's acceleration,  $\mathbf{a}_w$ , as well as the line's relative acceleration in both the tangential and normal directions,  $\mathbf{a}_{rel_t}$  and  $\mathbf{a}_{rel_n}$ , respectively, relative to the current. The drag force  $\mathbf{f}_D$  is calculated through

$$\mathbf{f}_D = \frac{1}{2} \frac{\rho_w d_0}{\sqrt{1 + \varepsilon}} \left( C_{D_t} \mathbf{v}_{rel_t} \|\mathbf{v}_{rel_t}\| + C_{D_n} \mathbf{v}_{rel_n} \|\mathbf{v}_{rel_n}\| \right). \quad (13)$$

The interactions between the sea bottom and the line are accounted for by using a linear stiffness spring-damper model for the vertical force  $\mathbf{f}_{C_n}$ , while a tangential friction model  $\mathbf{f}_{C_t}$  is applied when horizontal velocities are present, i.e.,

$$\mathbf{f}_{C_n} = k_{sb} d_0 (z_{sb} - r_z) - 2\beta_{sb} \sqrt{k_{sb} m_0 d_0} \min(\mathbf{v}_n, 0), \quad (14)$$

and

$$\mathbf{f}_{C_t} = \text{sgn}(\mathbf{v}_t) \mu_{sb} \tanh\left(\frac{\pi}{v_\mu} \mathbf{v}_t\right) \mathbf{f}_B. \quad (15)$$

Here,  $k_{sb}$  is the spring stiffness,  $\beta_{sb}$  is the damping coefficient,  $\mu_{sb}$  is the dynamic friction coefficient corresponding to a maximum friction velocity  $v_\mu$ , and  $\text{sgn}$  is the signum function. The model is applied whenever the vertical coordinate of a node  $r_z$  is in contact or below the sea bottom vertical coordinate  $z_{sb}$ . Moreover, the damping force is activated if and only if a ground node's velocity is negative (i.e., it is moving towards the sea bottom).

## 2.3. Bending and torsion

Bending and torsional moments on the line induce additional internal forces of the axial, shear and torsional types. An explicit formula for calculating this force can be derived from the angular momentum balance (Buckham et al., 2004). For typical mooring materials, rotary inertia, shear deformation, and distributed moments are negligible (Howell, 1992). These assumptions reduce angular momentum conservation to a quasi-static equilibrium, where the torsional and bending-induced force  $\mathbf{T}_b$  balances the internal moment on the cross-section  $\mathbf{M}$  (Tjavaras, 1996),

$$\frac{\partial}{\partial s} \left( \frac{\mathbf{M}}{(1 + \varepsilon)^2} \right) = (1 + \varepsilon) \hat{\mathbf{t}} \times \mathbf{T}_{bend}. \quad (16)$$

The moment  $\mathbf{M}$  can be written as (Landau and Lifshitz, 1975)

$$\mathbf{M} = (EI \hat{\mathbf{t}}) \times \boldsymbol{\kappa} + GI \gamma \hat{\mathbf{t}}, \quad (17)$$

where the bending stiffness  $EI$  and torsional rigidity  $GI$  are assumed constant. Moreover, the torsion angle is denoted by  $\gamma$ . For a mooring line with homogeneous circular cross-section, no torsion occurs for any bending moment; hence, torsion is constant along the segment if no external torques are applied.

We can isolate the bending-induced force  $\mathbf{T}_b$  by performing the cross-product with  $(-\hat{\mathbf{t}})$  on both sides of Eq. (16), yielding

$$\mathbf{T}_b = \frac{1}{1 + \varepsilon} \left[ \hat{\mathbf{t}} \times \frac{\partial}{\partial s} \left( \frac{\mathbf{M}}{(1 + \varepsilon)^2} \right) \right]. \quad (18)$$

Neglecting torsion effects, the derivative of the moment vector with respect to the coordinate  $s$  is

$$\frac{\partial}{\partial s} \left( \frac{\mathbf{M}}{(1 + \varepsilon)^2} \right) = \frac{EI}{(1 + \varepsilon)^2} \left( \hat{\mathbf{t}} \times \frac{\partial \boldsymbol{\kappa}}{\partial s} \right) - \frac{2EI}{(1 + \varepsilon)^3} \frac{\partial \varepsilon}{\partial s} (\hat{\mathbf{t}} \times \boldsymbol{\kappa}). \quad (19)$$

The assumption of a line with uniform properties along its length is maintained; hence, the bending stiffness  $EI$  and torsional rigidity  $GI$  do not depend on the unstretched coordinate  $s$ . Substituting

$$\mathbf{T}_b = \frac{\hat{\mathbf{t}}}{1 + \varepsilon} \times \left( \frac{EI}{(1 + \varepsilon)^2} \hat{\mathbf{t}} \times \frac{\partial \boldsymbol{\kappa}}{\partial s} \right) + \frac{\hat{\mathbf{t}}}{1 + \varepsilon} \times \left( -\frac{2EI}{(1 + \varepsilon)^3} \frac{\partial \varepsilon}{\partial s} \hat{\mathbf{t}} \times \boldsymbol{\kappa} \right), \quad (20)$$

or, using the triple cross-product and manipulating,

$$\mathbf{T}_b = \frac{EI}{(1 + \varepsilon)^3} \left[ \hat{\mathbf{t}} \left( \hat{\mathbf{t}} \cdot \frac{\partial \boldsymbol{\kappa}}{\partial s} \right) - \frac{\partial \boldsymbol{\kappa}}{\partial s} + \frac{2}{1 + \varepsilon} \frac{\partial \varepsilon}{\partial s} \boldsymbol{\kappa} \right]. \quad (21)$$

Several terms contribute to the force due to the bending force with different directions, scaling with the curvature  $\boldsymbol{\kappa}$  and the derivative of the curvature  $\partial \boldsymbol{\kappa}/\partial s$ . Furthermore, by accounting the spatial variation of strain in the derivation, a term that couples the strain gradient with the curvature is obtained. To incorporate Eq. (21) to our system, the curvature is added as an auxiliary variable  $\boldsymbol{\kappa}$  that is evolved in time, with

$$\frac{\partial \boldsymbol{\kappa}}{\partial t} = \frac{\partial}{\partial s} \left( \frac{\partial \hat{\mathbf{t}}}{\partial t} \right) = \frac{\partial}{\partial s} \left( \frac{1}{1 + \varepsilon} \frac{\partial \mathbf{q}}{\partial t} - \frac{\mathbf{q}}{(1 + \varepsilon)^2} \frac{\partial \varepsilon}{\partial t} \right) = \frac{\partial \mathbf{f}_\kappa}{\partial s}. \quad (22)$$

## 2.4. System of equations

Gathering terms, the complete system of equations for submerged mooring line dynamics in conservative form reads

$$\frac{\partial \mathbf{r}}{\partial t} = \mathbf{v}, \quad (23a)$$

$$\frac{\partial}{\partial t} (m_0 \mathbf{v}) = \frac{\partial}{\partial s} (T\hat{\mathbf{t}}) + \frac{\partial}{\partial s} (\mathbf{T}_b) + \mathbf{f}(1 + \varepsilon), \quad (23b)$$

$$\frac{\partial \mathbf{q}}{\partial t} = \frac{\partial \mathbf{v}}{\partial s}, \quad (23c)$$

$$\frac{\partial \mathbf{k}}{\partial t} = \frac{\partial}{\partial s} (\mathbf{f}_k). \quad (23d)$$

The above system can be expressed as a one-dimensional hyperbolic-parabolic balance law of the conserved variables  $\mathbf{U} \in \mathbb{R}^n$  ( $n = 4$ ),

$$\frac{\partial \mathbf{U}}{\partial t} + \frac{\partial \mathbf{F}_c}{\partial s} - \frac{\partial \mathbf{F}_d}{\partial s} = \mathbf{S}, \quad (24)$$

where

$$\mathbf{U}(s, t) = (\mathbf{r} \quad m_0 \mathbf{v} \quad \mathbf{q} \quad \mathbf{k})^T, \quad (25a)$$

$$\mathbf{F}_c(\mathbf{U}) = (\mathbf{0} \quad -T\hat{\mathbf{t}} \quad -\mathbf{v} \quad \mathbf{0})^T, \quad (25b)$$

$$\mathbf{F}_d\left(\mathbf{U}, \frac{\partial \mathbf{U}}{\partial s}\right) = (\mathbf{0} \quad T_b \quad \mathbf{0} \quad \mathbf{f}_k)^T, \quad (25c)$$

$$\mathbf{S}(\mathbf{U}) = (\mathbf{v} \quad (1+\varepsilon)\mathbf{f} \quad \mathbf{0} \quad \mathbf{0})^T, \quad (25d)$$

and  $s \in [0, L_0]$  and  $t \in \mathbb{R}^+$ , complemented with well-posed boundary conditions. The fluxes are divided into a convective flux  $\mathbf{F}_c$  term dependent on the solution and a diffusive flux term  $\mathbf{F}_d$ , that depends on the solution and its derivative.

The diffusive part of the equation can be neglected for chains and wires. When the diffusive terms are neglected in Eq. (24), the system is hyperbolic since the Jacobian  $\partial \mathbf{F}_c / \partial \mathbf{U}$  has distinct and real eigenvalues (Cristescu, 2007). Applying a similarity transformation to  $\partial \mathbf{F}_c / \partial \mathbf{U}$  the following eigenvalues matrix is obtained

$$\boldsymbol{\lambda} = \text{diag}(-c_n \quad -c_n \quad c_n \quad c_n \quad -c_t \quad c_t), \quad (26)$$

where

$$c_t = \sqrt{\frac{1}{m_0} \frac{\partial T}{\partial e}}, \quad (27a)$$

$$c_n = \sqrt{\frac{T}{m_0(1+\varepsilon)}}, \quad (27b)$$

are the tangential and normal wave speeds propagated in the line, respectively.

### 3. Discontinuous Galerkin spectral element method

Consider systems of convection-diffusion balance laws in a one-dimensional domain defined by Eq. (24), subject to a suitable set of initial and boundary conditions. To discretise the system, a Legendre-Gauss-Lobatto DG spectral element method (LGL-DGSEM) formulation is used (Gassner et al., 2016). This scheme is a nodal collocation variant of the DG method, where the interpolation nodes are collocated at the LGL quadrature nodes in the reference space. This is demonstrated summarily below. Detailed derivations are referred to Hesthaven and Warburton (2008), Kopriva (2009). The diffusive terms are addressed in Section 3.4.

#### 3.1. Discretisation

The DG method is assembled through a decomposition of the computational domain  $\Omega(s) = [0, L_0]$  into  $M$  non-overlapping elements  $\Omega_m$ , such that  $\Omega = \bigcup_{m=1}^M \Omega_m$ , where  $\Omega_m = [s_m, s_{m-1}]$  and  $\Delta s_m = (s_m - s_{m-1})$ . For each element  $\Omega_m$ , it is convenient to construct a linear invertible mapping  $\xi = \xi(s)$  to a reference space  $E(\xi) = [-1, 1]$ , through

$$s(\xi) = s_{m-1} + \frac{\Delta s_m}{2}(\xi + 1). \quad (28)$$

The spatial derivatives concerning the physical domain  $s$  are transformed into the reference spatial coordinate  $\xi$ ,

$$\frac{\partial}{\partial s}(\cdot) = \frac{ds}{d\xi} \frac{\partial}{\partial \xi}(\cdot) = J_m^{-1} \frac{\partial}{\partial \xi}(\cdot), \quad (29)$$

where the Jacobian of the mapping is as  $J_m = \frac{ds}{d\xi} = \frac{\Delta s_m}{2}$ , Thus, for each element  $m$ , a transformed system of equations is solved in the reference coordinates with

$$J_m \frac{\partial \mathbf{U}_m}{\partial t} + \frac{\partial \mathbf{F}_m}{\partial \xi} = J_m \mathbf{S}_m, \quad (30)$$

$$\text{where } \mathbf{F}_m = \mathbf{F}_{c_m} - \mathbf{F}_{d_m}.$$

#### 3.2. Weak form

A uniformly spaced grid leads to  $J_m = J$ . The DG method is based on a local weak-type Galerkin finite-element approach. To obtain the equations, each element's balance law must be rewritten into its weak (or variational) formulation. Moreover, the test/trial functions are the same as the basis functions used to approximate the piecewise solutions. Using Lagrangian basis functions  $\ell(\xi)$  for each element, the solution is approximated by a polynomial interpolant of order  $N$ , written in nodal form as follows

$$\mathbf{U}(s(\xi), t) \approx \mathbf{U}_N(\xi, t) = \sum_{j=0}^N \hat{U}_j(t) \ell_j(\xi), \quad (31)$$

where  $\hat{U}_j$  are the  $N + 1$  time-dependent degrees of freedom. The one-dimensional Lagrange polynomial functions  $\ell_j(\xi)$  are defined by

$$\ell_j(\xi) = \prod_{i=0, i \neq j}^N \frac{\xi - \xi_i}{\xi_j - \xi_i}, \quad (32)$$

for  $i, j = 0, \dots, N$ , with the cardinal property at the interpolation nodes

$$\ell_j(\xi_i) = \delta_{ij}, \quad (33)$$

where  $\delta_{ij}$  is the Kronecker delta. Finding the unknown coefficients is equivalent to determining the values of the nodal points since

$$\mathbf{U}_N(\xi_i, t) = \sum_{j=0}^N \hat{U}_j(t) \ell_j(\xi_i) = \sum_{j=0}^N \hat{U}_j(t) \delta_{ij} = \hat{U}_i. \quad (34)$$

Before substituting, the variational formulation in the global domain is first written as the sum of  $k$  local ones in the partitioned grid,

$$\int_{-1}^1 \ell_i \left( J \frac{\partial \mathbf{U}}{\partial t} + \frac{\partial \mathbf{F}}{\partial \xi} \right) d\xi = \int_{-1}^1 J \ell_i \mathbf{S} d\xi, \quad (35)$$

where  $i = 0, 1, \dots, N$  in what follows, unless stated otherwise. Integrating the flux derivative term by parts yields the DG in weak form

$$J \int_{-1}^1 \ell_i \frac{\partial \mathbf{U}}{\partial t} d\xi - \int_{-1}^1 \frac{d\ell_i}{d\xi} \mathbf{F} d\xi + [\ell_i \mathbf{F}^*]_{-1}^1 = J \int_{-1}^1 \ell_i \mathbf{S} d\xi, \quad (36)$$

where the surface flux is replaced by a consistent numerical flux function  $\mathbf{F}^*$  because, in contrast to a continuous FEM, there is an indeterminate surface flux function at the interface. Instead, the continuity is enforced in a weak sense by approximately solving the Riemann problem at the interface, as in a finite-volume method, with a numerical flux function that depends on the left and right states, i.e.,  $\mathbf{F}^*(\mathbf{U}) = \mathbf{F}^*(\mathbf{U}^-, \mathbf{U}^+)$ . Boundary conditions are also weakly imposed through the Riemann solver (see Section 3.6). Note that this methodology does not readily handle diffusive fluxes that depend on the derivative of the solution; see Section 3.4 for further details.

##### 3.2.1. LGL nodes and collocation

The LGL nodes are  $\xi = \pm 1$  and the  $N - 1$  roots of the  $N^{\text{th}}$  order Legendre polynomial. These nodes include the boundaries and are appropriate for interpolation and numerical integration. Therefore, the integrals in the DG formulation in Eq. (36) are computed using a Gauss-Lobatto integration rule,

$$\int_{-1}^1 g(\xi) d\xi \approx \sum_{m=0}^N \omega_m g(\xi_m), \quad (37)$$

where  $\xi_m$  and  $\omega_m$  are the LGL quadrature points and weights, respectively. The maximum polynomial order precision for the LGL quadrature is  $2N - 1$ ; a Gaussian quadrature offers precision up to  $2N + 1$  but there is the computational cost of solution data being interpolated to the boundary (Canuto, 2006). Compared to the Gaussian quadrature, the LGL variant has an increased time step advantage and is more computationally efficient (Gassner and Kopriva, 2011).

Using collocation with a unique set of LGL nodes, the discrete orthogonality in  $L_2(-1, 1)$  of the Lagrangian basis functions is exploited. This enables highly efficient 1D discrete operators (Karniadakis and Sherwin, 2005) with special properties, as shown next. Besides the solution, the fluxes and source terms are also collocated.

### 3.2.2. LGL-DGSEM

Each entry of the vector of conservative variables

$$\mathbf{U} = (U_1 \quad \dots \quad U_k \quad \dots \quad U_n)^T, \quad (38)$$

can be written as

$$U_k = \sum_{j=0}^N \ell_j(\xi) \hat{U}_{k,j}. \quad (39)$$

Similarly, each entry  $k$  of the vectors of convective fluxes and source terms can be written as

$$F_k = \sum_{j=0}^N \ell_j(\xi) \hat{F}_{k,j}, \quad (40)$$

and

$$S_k = \sum_{j=0}^N \ell_j(\xi) \hat{S}_{k,j}. \quad (41)$$

Solving Eq. (36) for a single variable  $\hat{\mathbf{U}}_k$  yields

$$\begin{aligned} \sum_{j=0}^N J \int_{-1}^1 \ell_i(\xi) \ell_j(\xi) \frac{\partial \hat{U}_{k,j}}{\partial t} d\xi - \sum_{j=0}^N \int_{-1}^1 \frac{d\ell_i}{d\xi}(\xi) \ell_j(\xi) \hat{F}_{k,j} d\xi \\ + [\ell_i F_k^*]_{-1}^1 = \sum_{j=0}^N J \int_{-1}^1 \ell_i(\xi) \ell_j(\xi) \hat{S}_{k,j} d\xi. \end{aligned} \quad (42)$$

The discrete mass matrix  $\mathbf{M}$  and the stiffness matrix  $\mathbf{Q}$  are

$$\begin{aligned} M_{ij} &= \int_{-1}^1 \ell_i(\xi) \ell_j(\xi) d\xi \\ &\approx \sum_{m=0}^N \omega_m \ell_i(\xi_m) \ell_j(\xi_m) \\ &= \sum_{m=0}^N \omega_m \delta_{im} \delta_{jm} = \omega_i \delta_{ij}, \end{aligned} \quad (43)$$

and

$$\begin{aligned} Q_{ij} &= \int_{-1}^1 \frac{d\ell_i}{d\xi}(\xi) \ell_j(\xi) d\xi \\ &\approx \sum_{m=0}^N \omega_m \frac{d\ell_i}{d\xi}(\xi_m) \ell_j(\xi_m) \\ &= \sum_{m=0}^N \omega_m \frac{d\ell_i}{d\xi}(\xi_m) \delta_{jm} = \omega_j \frac{d\ell_i}{d\xi}(\xi_j). \end{aligned} \quad (44)$$

Here, property (33) is used. The mass matrix is diagonal with positive weights for all polynomial orders; hence, it can be easily inverted (Hesthaven and Warburton, 2008). The discrete stiffness matrix  $\mathbf{Q}$  contains the weighted derivatives of the Lagrangian basis at the interpolation/quadrature nodes. The matrix entries are a function of the nodal points and barycentric weights (Kopriva, 2009). Again, the weak form derivative matrix (polynomial of order  $2N - 1$ ) is computed exactly and an error is incurred in evaluating the mass matrix (polynomial of order  $2N$ ) due to the insufficient precision of the LGL quadrature. This

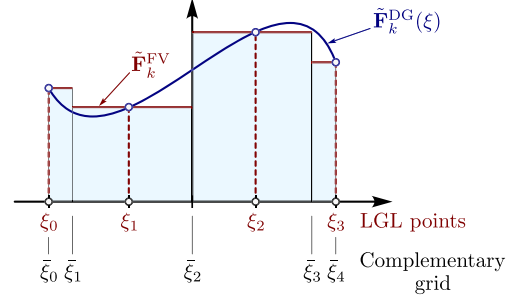


Fig. 2. LGL grid and complementary grid used in the DGSEM/FV scheme.

type of aliasing error is known as “mass lumping” in spectral methods (Canuto, 2006). For well-behaved solutions, this error decays spectrally (Karniadakis and Sherwin, 2005).

Using the definitions (43) and (44), we can substitute into Eq. (42) yielding

$$\sum_{j=0}^N J M_{ij} \frac{\partial \hat{U}_{k,j}}{\partial t} - \sum_{j=0}^N Q_{ij} \hat{F}_{k,j} + \delta_{iN} F_k^*(\xi_N) - \delta_{i0} F_k^*(\xi_0) = \sum_{j=0}^N J M_{ij} \hat{S}_{k,j}, \quad (45)$$

or, in matrix-vector form,

$$J \mathbf{M} \frac{\partial \mathbf{U}_k}{\partial t} - \mathbf{Q} \mathbf{F}_k + \mathbf{B} \mathbf{F}_k^* = J \mathbf{M} \mathbf{S}_k, \quad (46)$$

where

$$\mathbf{B} = \text{diag} (-1 \quad 0 \quad \dots \quad 0 \quad 1), \quad (47a)$$

$$\mathbf{U}_k = (\hat{U}_k(\xi_0) \quad 0 \quad \dots \quad 0 \quad \hat{U}_k(\xi_N))^T, \quad (47b)$$

$$\mathbf{F}_k = (\hat{F}_k(\xi_0) \quad 0 \quad \dots \quad 0 \quad \hat{F}_k(\xi_N))^T, \quad (47c)$$

$$\mathbf{S}_k = (\hat{S}_k(\xi_0) \quad 0 \quad \dots \quad 0 \quad \hat{S}_k(\xi_N))^T, \quad (47d)$$

$$\mathbf{F}_k^* = (F_k^*(\xi_0) \quad 0 \quad \dots \quad 0 \quad F_k^*(\xi_N))^T. \quad (47e)$$

Let us define the matrix

$$D_{ij} = \frac{d\ell_j}{d\xi}(\xi_i), \quad (48)$$

such that  $\mathbf{Q}^T = \mathbf{MD}$ . The discrete operators of the DGSEM satisfy the Summation-By-Parts (SBP) property for all polynomial orders (Carpenter and Gottlieb, 1996),

$$\mathbf{Q}^T + \mathbf{Q} = \mathbf{MD} + (\mathbf{MD})^T = \mathbf{B}. \quad (49)$$

With property (49), multiple expressions for the derivative matrix can be written. Substituting in Eq. (46), we get

$$\begin{aligned} J \mathbf{M} \frac{\partial \mathbf{U}_k}{\partial t} &= (\mathbf{MD})^T \mathbf{F}_k - \mathbf{B} \mathbf{F}_k^* + J \mathbf{M} \mathbf{S}_k \\ &= (\mathbf{B} - \mathbf{MD}) \mathbf{F}_k - \mathbf{B} \mathbf{F}_k^* + J \mathbf{M} \mathbf{S}_k \\ &= -\mathbf{MDF}_k - \mathbf{B} (\mathbf{F}_k^* - \mathbf{F}_k) + J \mathbf{M} \mathbf{S}_k. \end{aligned} \quad (50)$$

After manipulation,

$$\frac{\partial}{\partial t} (\mathbf{U}_k^{\text{DG}}) = -\frac{1}{J} [\mathbf{DF}_k - \mathbf{M}^{-1} \mathbf{B} (\mathbf{F}_k^* - \mathbf{F}_k)] + \mathbf{S}_k = \tilde{\mathbf{F}}_k^{\text{DG}} + \mathbf{S}_k^{\text{DG}}. \quad (51)$$

This corresponds to the second integration-by-parts of the volume term of the weak form, that is, the DG strong form for each LGL node  $j$ . It shows that the LGL-DGSEM has discretely equivalent weak and strong forms (Kopriva and Gassner, 2010).

### 3.3. Shock capturing

#### 3.3.1. Complementary grid

Fisher and Carpenter (2013) proved that the subclass of diagonal norm SBP discretisations from which LGL-DGSEM belong can express the volume integral term (50) as an algebraically equivalent telescoping

flux-differencing formulation. This leads to an interpretation of the LGL-DGSEM as a subcell FV-type flux-difference scheme, with a subdivision of each element into  $N + 1$  inner cells spaced with a width equal to the LGL quadrature weights  $\omega_i$  (Rueda-Ramírez et al., 2021), as shown in Fig. 2. Following those authors, a set of  $N + 2$  complementary flux points  $\xi$  is introduced, that define the boundaries of control volumes surrounding each solution point,

$$\xi = (\xi_0 \quad \xi_1 \quad \dots \quad \xi_{N+2})^T, \quad (52)$$

with  $\xi_0 = \xi_0$  and  $\xi_{N+2} = \xi_{N+1}$ . Thus, the solution and flux points coincide at the boundaries. These points establish a grid defined by the following matrix-vector notation

$$\Delta \xi = \mathbf{M} \mathbf{1}, \quad (53)$$

where  $\mathbf{1} = (1 \quad 1 \quad \dots \quad 1)^T$  and

$$\Delta = \begin{pmatrix} -1 & 1 & 0 & \dots & \dots & 0 \\ 0 & -1 & 1 & 0 & \dots & 0 \\ \vdots & \ddots & \ddots & \ddots & \ddots & \vdots \\ 0 & \dots & 0 & -1 & 1 & 0 \\ 0 & \dots & \dots & 0 & -1 & 1 \end{pmatrix}, \quad (54)$$

and, hence, the distance between flux points is dictated by the diagonal entries of  $\mathbf{M}$ .

### 3.3.2. The blended DGSEM-FV scheme

To handle shocks, an appropriate scheme to combat the spurious oscillations inherent of local high-order polynomial approximations is needed. This can be achieved by a low-order scheme, dissipative enough to be robust in the presence of discontinuities. In this work, a finite-volume subcell framework is used (Persson and Peraire, 2006; Hennemann et al., 2021). The main idea is the local blending of a high-order DG method with a compatible FV subcell method, i.e.,

$$\frac{\partial}{\partial t} (\mathbf{U}_k^{DG/FV}) = (1 - \alpha) \tilde{\mathbf{F}}_k^{DG} + \alpha \tilde{\mathbf{F}}_k^{FV} + \mathbf{S}_k^{DG}. \quad (55)$$

The utilization of FV subcells appears quite naturally considering the interpretation provided by Fisher et al. (2013) and Fisher and Carpenter (2013) explained in Section 3.3.1. The flux-differencing form is applicable since the LGL-DSGEM is a diagonal-norm SBP operator. The compatible subcell FV method treats the LGL nodal values as cell-centred mean values in the grid (54), despite the LGL nodes not being geometrically centred. Hence,

$$\frac{\partial}{\partial t} (\mathbf{U}_k^{FV}) = -\frac{1}{J\omega_i} (\mathbf{F}_{k(i,i+1)}^{FV} - \mathbf{F}_{k(i-1,i)}^{FV}) = \tilde{\mathbf{F}}_k^{FV}, \quad (56)$$

with approximate Riemann solvers at the subcell interfaces,  $\mathbf{F}_{k(i,i+1)}^{FV} = \mathbf{F}_k^*(\mathbf{U}_i, \mathbf{U}_{i+1})$ . External boundary conditions give the numerical fluxes at the domain edges, just as in the high-order DGSEM. Therefore, Eq. (55) consists of an elementwise convex combination of both residuals through a single-element piecewise blending coefficient  $\alpha$ . Note that the discretisation schemes are being blended, not the solutions.

A simplified pseudo-code of the blended scheme is shown in Algorithm 1.

### 3.3.3. Blending coefficient

The computation of the blending coefficient is based on a shock indicator function (e.g., Persson and Peraire (2006), Klöckner et al. (2011)) computed before each timestep. This function should properly recognize discontinuities, marking the troubled elements accordingly.

Following the framework presented in Hennemann et al. (2021), the local blending factor  $\alpha \in [0, 1]$  is calculated based on the modal energy contained in the high-order polynomial modes of a physical quantity  $\epsilon$ , compared to the overall modal energy. The indicator quantity  $\epsilon$  is expressed using the hierarchical Legendre polynomial space  $L_j(\xi)$  derived from the collocated nodal representation,

$$\epsilon(\xi) = \sum_{j=0}^N \epsilon_j \ell_j(\xi) = \sum_{j=0}^N \hat{\epsilon}_j L_j(\xi), \quad (57)$$

---

### Algorithm 1 Blended DGSEM-FV scheme.

---

```

1: procedure  $\frac{\partial}{\partial t}(\mathbf{U})$ 
2:   for each element  $\Omega_e$  do
3:     Compute flux gradient  $\frac{\partial \mathbf{F}}{\partial s}(\mathbf{U}, \frac{\partial \mathbf{U}}{\partial s})$ :
4:     Compute blending coefficient  $\alpha$  using (59)
5:     Compute high-order flux contribution from DG kernel (51)
6:     Compute low-order flux contribution from FV kernel (56)
7:     Apply boundary conditions, if on domain edge.
8:     Blend contributions  $\frac{\partial \mathbf{U}}{\partial t} = (1 - \alpha) \frac{\partial \mathbf{U}^{DG}}{\partial t} + \alpha \frac{\partial \mathbf{U}^{FV}}{\partial t}$ 
9:     Apply Jacobian
10:    Add source terms:  $\frac{\partial \mathbf{U}}{\partial t} = \frac{\partial \mathbf{U}}{\partial t} + \mathbf{S}$ 
11:   end for
12: end procedure

```

---

where  $\hat{\epsilon}_j$  are the modal coefficients from the Legendre polynomials  $L_j$ . The relative energy in each DG element with is computed as

$$\tilde{E} = \max \left\{ \frac{\hat{\epsilon}_N^2}{\sum_{i=0}^N \hat{\epsilon}_i^2}, \frac{\hat{\epsilon}_{N-1}^2}{\sum_{i=0}^{N-1} \hat{\epsilon}_i^2} \right\} \quad (58)$$

where the denominator consists of the modal energy of a one-dimensional polynomial. The two highest modal energies are considered to avoid odd/even effects when approximating local functions. The calculated relative energy is then compared with a threshold  $\tilde{T}$  based on the expected decay of the modal coefficients for smooth solutions

$$\tilde{T}(N) = a \cdot 10^{-c(N+1)^{\frac{1}{4}}},$$

where  $a = 0.5$  and  $c = 1.8$  (Hennemann et al., 2021). At the beginning of each Runge-Kutta stage, the blending coefficient is computed for all elements based on the energy mode indicator  $\tilde{E} \in [0, 1]$  and threshold  $\tilde{T}$ , using

$$\alpha = \frac{1}{1 + \exp(-s(\frac{\tilde{E}}{\tilde{T}} - 1))}, \quad (59)$$

with  $s = 9.21024$  such that  $\alpha(\tilde{E} = 0) = 0.0001$ . Note that  $\alpha = 0$  corresponds to pure DGSEM, while  $\alpha = 1$  corresponds to pure FV. It is more efficient to adjust the value of the blending coefficient when close to both limits of the interval (pure DG/FV) as follows,

$$\alpha = \begin{cases} 0, & \text{if } \alpha < \alpha_{\min}, \\ \alpha, & \text{if } \alpha_{\min} \leq \alpha \leq \alpha_{\max}, \\ \alpha_{\max}, & \text{if } \alpha_{\max} < \alpha. \end{cases} \quad (60)$$

while also choosing the amount of robustness needed for the application. The  $\alpha_{\min}$  and  $\alpha_{\max}$  are decided heuristically, requiring trial and error and/or experience for each user case. Finally, the local values of  $\alpha$  are diffused with the neighbouring elements  $e$ ,

$$\alpha = \max_e \{\alpha, 0.5\alpha_e\}, \quad (61)$$

to create a smoother transition between elements. For a more complete algorithm description, see Hennemann et al. (2021). For other variants and applications of the DG-FV blended formulation, consult Markert et al. (2023), Potluri et al. (2023).

For the results presented in Section 4, the tension force magnitude was chosen as the indicator function, with a maximum value of  $\alpha = 0.5$  and a minimum of  $\alpha = 0.01$ .

### 3.4. Approximation of diffusion terms

Second-order derivatives arise from the diffusive flux gradient that contains first-order terms. These are difficult to incorporate directly into the weak formulation in a discontinuous polynomial space. The impact of interface discontinuities on the solution's derivative must be considered to achieve a consistent and stable discretisation of the diffusive

**Table 1**

Dirichlet, Neumann and mixed boundary conditions for typical mooring line ends. The index “bc” indicates a prescribed value while the superscript “-” indicates values from the interior of the boundary interface.

Type / Variable	$\hat{t}$	$v$	$\kappa$	$T$	$f_\kappa$
Clamped	$\hat{t}_{bc}$	0	$\kappa^-$	$T^-$	0
Kinematic	$\hat{t}^-$	$v_{bc}$	0	$T^-$	$f_\kappa^-$
Pinned	$\hat{t}^-$	0	$\kappa^-$	$T^-$	$f_\kappa^-$
Free	$\hat{t}^-$	$v^-$	0	0	$f_\kappa^-$

fluxes. Several techniques are available for discretising the diffusive terms using a DG method. A comprehensive review is found in Arnold et al. (2002).

In this work, the discretisation of the second-order diffusive terms is handled by a mixed finite-element formulation. The gradient in the weak formulation is discretised introducing the derivative itself as an auxiliary variable (Bassi and Rebay, 1997),

$$\mathbf{G} - \frac{\partial \mathbf{U}}{\partial s} = \mathbf{0}. \quad (62)$$

The same approximation polynomial basis functions are used for the solution for the gradient variables. The DG weak form is

$$J \int_{-1}^1 \ell_i \mathbf{G} d\xi + \int_{-1}^1 \frac{\partial \ell_i}{\partial \xi} \mathbf{U} d\xi + [\ell_i \mathbf{U}^*]_{-1}^1 = 0. \quad (63)$$

Similarly to what was done before, the unknown interface solution is replaced with a numerical flux function  $\mathbf{U}^*$  since the solution is discontinuous. For both the gradient equation and diffusion flux term in the original one, the average/arithmetic mean is used as the surface flux,

$$\mathbf{U}^*(\mathbf{U}) = \mathbf{U}^*(\mathbf{U}^+, \mathbf{U}^-) = \frac{1}{2}(\mathbf{U}^+ + \mathbf{U}^-). \quad (64)$$

and

$$\mathbf{F}^*(\mathbf{U}) = \mathbf{F}^*(\mathbf{U}^+, \mathbf{F}^-) = \frac{1}{2}(\mathbf{F}^+ + \mathbf{F}^-). \quad (65)$$

The numerical flux function must be consistent with the boundary conditions of the problem at the boundaries. Moreover, an explicit time integration scheme greatly simplifies the procedure. Although this approach is general and straightforward to implement, it has the drawback of requiring additional calculation and storage of the first-order derivatives.

### 3.5. Numerical flux

The numerical fluxes are computed using the local Lax-Friedrichs flux,

$$\mathbf{F}_c^*(\mathbf{U}) = \frac{1}{2}(\mathbf{F}(\mathbf{U}^+) + \mathbf{F}(\mathbf{U}^-)) - \frac{1}{2}\lambda_{\max}(\mathbf{U}^+ - \mathbf{U}^-). \quad (66)$$

where  $\lambda_{\max}$  corresponds to the local absolute maximum eigenvalue of Eq. (26).

### 3.6. Boundary conditions

Boundary conditions are imposed weakly by specifying the numerical flux at domain boundaries. This is consistent with the variational structure of DG methods, enabling stable and high-order accurate solutions even in the presence of complex or discontinuous boundary data. Moreover, since boundary conditions enter the formulation through the same flux interface as interior elements, introducing new boundary types typically requires only localized modifications to the flux definition, facilitating implementation. Table 1 describes the different types of boundary condition implementations considering typical mooring problems.

### 3.7. Time discretisation

The semidiscrete DG formulation results in the system of ODEs (55). This system is then combined with a standard finite-difference numerical technique to integrate the time derivative, usually an explicit or implicit ODE solver. Here, the hybrid DG/FV scheme is integrated using explicit high-order strong stability-preserving (SSP) Runge-Kutta schemes (Shu and Osher, 1988), particularly the 4<sup>th</sup>-order Runge-Kutta method. The time step size is dictated by the Courant-Friedrichs-Lowy (CFL) condition (Courant et al., 1928),

$$\Delta t = \min \left( \text{CFL} \frac{\Delta s_{\min}}{(N+1)\lambda_{\max}} \right), \quad (67)$$

where  $\text{CFL} \leq 1$ . Moreover,  $\lambda_{\max}$  is the local maximal wave speed and  $\Delta s$  is the element size. Usually,  $\text{CFL} = 0.5$  is sufficient for stability.

## 4. Numerical examples

In this section, the results of the DGSEM model were compared against published analytical, numerical, and experimental results. Several test cases were considered, namely:

- Taut vibrating string
- Vibrating cantilever beam
- The swinging motion of a pinned cable from Koh et al. (1999)
- Catenary mooring chains from Bergdahl et al. (2016) and Barrera et al. (2019)

Appropriate sensitivity evaluations of simulation characteristics, such as element size, were conducted for all test cases, ensuring the accuracy of the numerical results. This is explicitly shown for the experimental catenary mooring chain test case (Section 4.4), in Section 4.4.2. For cases with analytical solution, the error analysis is done with the  $L_2$ -norm of the absolute error  $\|\mathbf{e}\|_{L_2}$ . For cases with no analytical solution, the initial conditions of the line are taken from a static analysis.

### 4.1. Taut vibrating string

The first benchmark for analytical validation is the vibrating string problem. It considers a string of uniformly constant mass per meter  $m_0$ , extended between two horizontally aligned fixed endpoints. The applied strain  $\varepsilon_0$  and tensile force  $T_0$  on the string is, thus, constant in space and time. A simplified form of the string dynamics equation is derived when small displacements are considered and coincides with the one-dimensional linear wave equation (Governo et al., 2023), for which there is an analytical solution (Greiner, 2010). The imposed initial conditions are: unstretched string length  $L_0 = 100$  m, mass (per meter)  $m_0 = 0.1$  kg/m and pre-tension force  $T_0 = 1100$  N, which is equivalent to an initial strain  $\varepsilon_0 = 0.1$ . The initial configuration of the string corresponds to  $r(s, 0) = \sin(\pi s/L_0)$ .

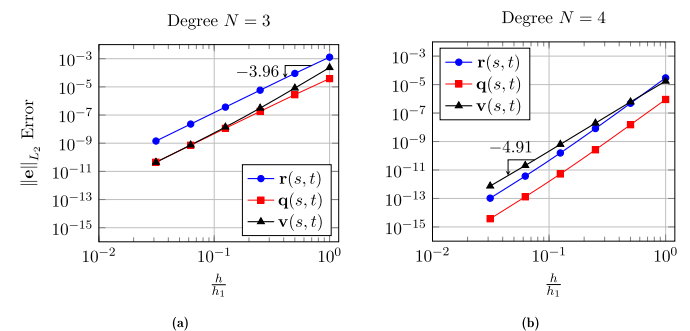
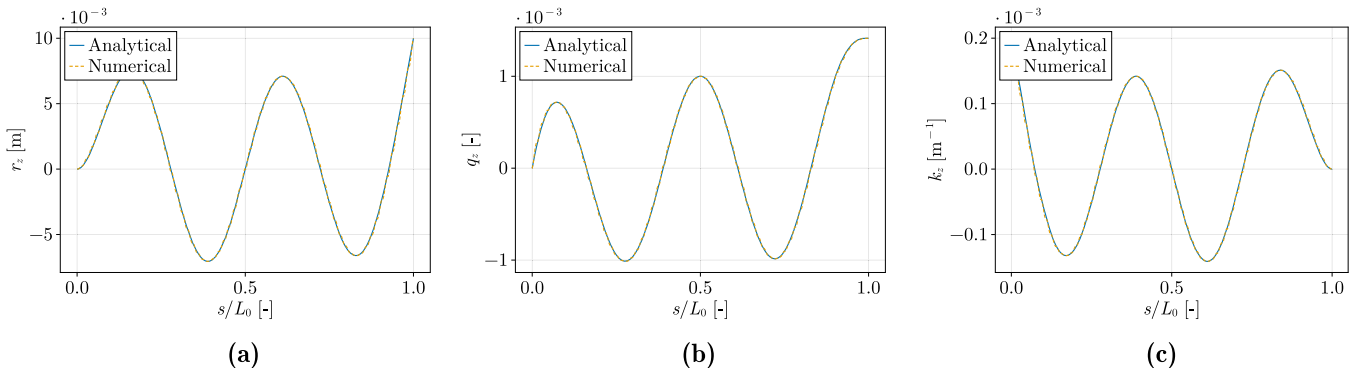
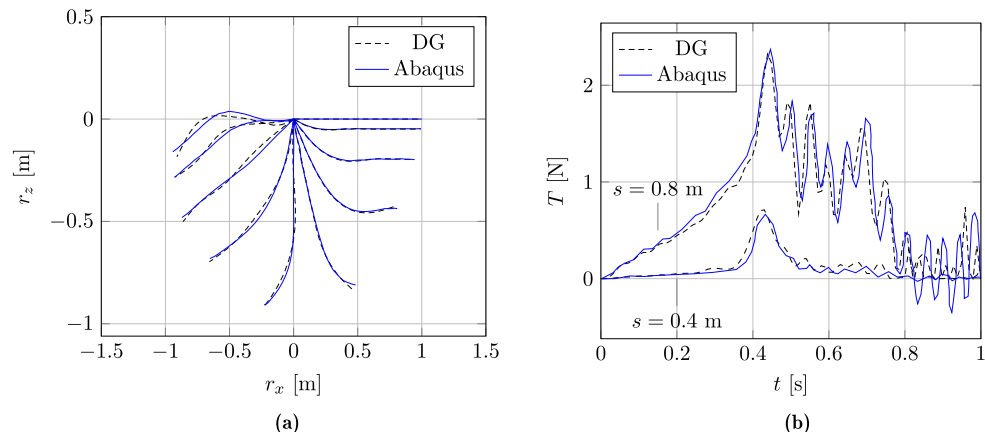


Fig. 3. Absolute error  $\|\mathbf{e}\|_{L_2}$  for the vibrating string problem.  $h_1$  is the element size of the coarsest mesh.



**Fig. 4.** Comparison between the analytical and DG numerical solutions for the vibrating cantilever problem, considering a) transverse displacement  $r = r_z$ , b) the displacement spatial derivative  $q_z$  and c) curvature  $\kappa_z$ .



**Fig. 5.** Comparison of results between the DG method and software *Abaqus*, for a) cable position  $r$  and b) axial force magnitude  $T$ . The position of cable is spaced between  $\Delta t = 0.1s$ , for  $t \in [0, 1]$ , where  $t = 0$  is the releasing of the cable. The evolution of tension in time is measured at  $s/L_0 = 0.4$  and  $s/L_0 = 0.8$ .

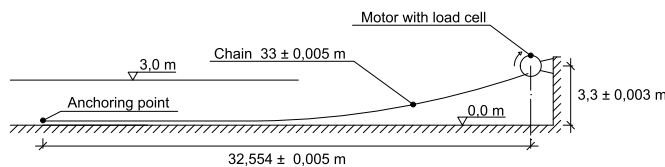


**Fig. 6.** Schematics of the experimental setup (Bergdahl et al., 2016).

**Table 2**  
Numerical model parameters for the vibrating beam problem.

Amplitude, $A$ [m]	0.01
Length, $L_0$ [m]	100
Mass per unit meter, $m_0$ [kg/m]	10
Axial stiffness, $EA_0$ [N]	$10^5$
Bending stiffness, $EI$ [N]	$10^5$

The results are shown in Fig. 3, for increasing the number of DOFs/elements and at different polynomial degrees, for a CFL = 0.45. The solution obtained by the analytical formula above is compared with the numerical one after one period of oscillation. It shows excellent agreement with the analytical solution and demonstrates the  $N + 1$  optimal convergence order expected from the method.

#### 4.2. Vibrating cantilever beam

The validation of the bending modelling is assessed through the problem of a free-vibrating Euler-Bernoulli beam. The governing equations of motion for the forced transverse vibration of a uniform Euler-Bernoulli

**Table 3**

$L_2$ -error norm and convergence rates for the vibrating cantilever test case after a complete vibration period.  $m$  is the number of elements in the grid.

$N = 3$					
$m$	$r_z$ [m]		$v_z$ [m/s]		$k_z$ [ $\text{m}^{-1}$ ]
	$\ \mathbf{e}\ _{L_2}$	rate	$\ \mathbf{e}\ _{L_2}$	rate	$\ \mathbf{e}\ _{L_2}$
4	5.3E-4	—	6.5E-3	—	9.8E-3
8	1.6E-5	5.05	2.2E-4	4.92	3.2E-7
16	9.9E-7	3.99	1.7E-5	3.87	2.2E-8

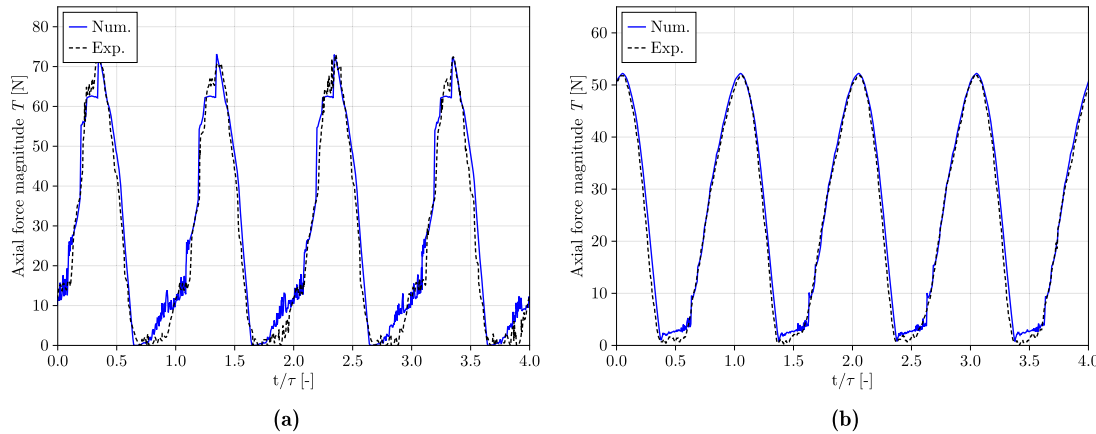
  

$N = 4$					
$m$	$r_z$ [m]		$v_z$ [m/s]		$k_z$ [ $\text{m}^{-1}$ ]
	$\ \mathbf{e}\ _{L_2}$	rate	$\ \mathbf{e}\ _{L_2}$	rate	$\ \mathbf{e}\ _{L_2}$
4	2.9E-5	—	8.7E-4	—	6.4E-7
8	1.5E-6	4.26	3.3E-5	4.74	2.9E-8
16	6.5E-8	4.51	3.2E-6	3.34	3.4E-9

beam with constant properties are

$$c^2 \frac{\partial^4 r}{\partial x^4}(x, t) + \frac{\partial^2 r}{\partial t^2}(x, t) = 0, \quad (68)$$

with  $c = \sqrt{EI/m_0}$ . Here,  $m_0 = \rho A_0$  is the mass per unit length ( $A_0$  is the cross-sectional area and  $\rho$  is the mass per unit of volume),  $I$  is the moment of inertia of the cross-sectional area,  $E$  is the modulus of elasticity and  $r(x, t)$  is the transverse deflection. The problem of transverse vibration in beams is characterized as an initial boundary value problem, and its analytical solution is found through variable separation



**Fig. 7.** Numerical and experimental results for the magnitude of the axial force measured at the upper-end for the test case with a) period  $\tau = 1.25$  s and b) period  $\tau = 3.50$  s and circular radius of  $R = 0.200$  m.

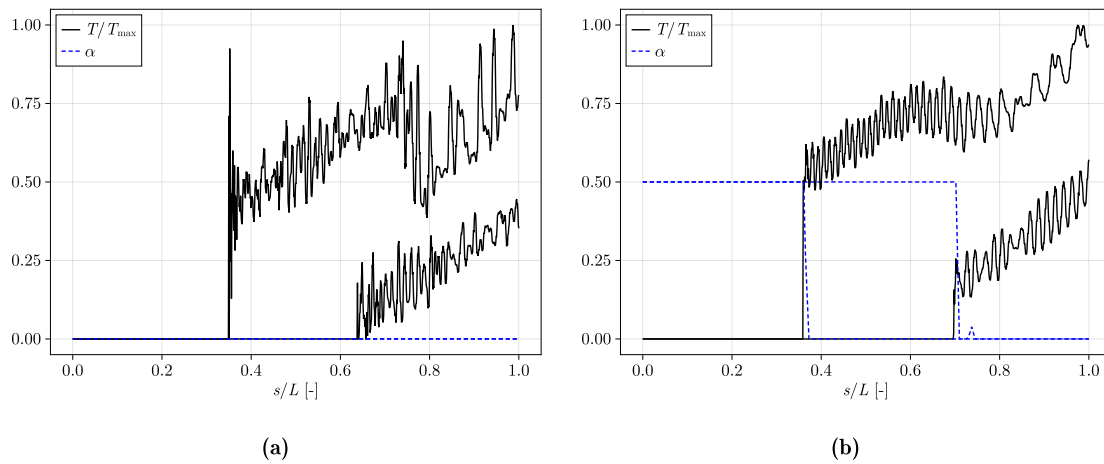


**Fig. 8.** Influence of the blending coefficient  $\alpha$  on the slack interval of the periodic catenary motion, at two different time instants, and for the nondimensional tension force magnitude along the line.

methods (Rao, 2011). A solution is given by  $r_z(s, t) = A W_n(s) \cos(\omega_n t)$ , with  $s \in [0, L_0]$  and  $t \geq 0$ . The value of the mode shape function  $W_n$  depends on the boundary conditions and the mode of free vibration; see Rao (2011) in Section 8.5 for more details. For this case, the 4<sup>th</sup> mode of vibration is considered, with beam properties based on Palm and Eskilsson (2020) and presented in Table 2. A clamped boundary condition is applied at the left end ( $r_x = 0$ ), while the right end ( $r_x = L_0$ ) is free.

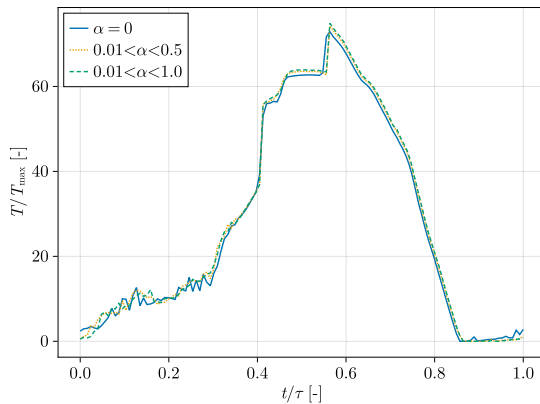


**Fig. 9.** Tension time-series over a complete motion cycle at the fairlead, for different values of blending coefficient.

This means there is no deflection and no slope at the clamped end, while there are no forces or moments at the free end.

To solve this equation numerically using the DG method, the beam is discretised by  $m = 16$  polynomials of order  $N = 4$ , and the simulation is conducted with a CFL = 0.1. The results are plotted in Fig. 4, after a vibration period. The  $L_2$  norm of the error and the convergence rates are shown in Table 3. The results are in agreement with the analytical solution and adequate dynamic behaviour is captured for all the relevant variables. The convergence rates show the optimal convergence for all orders tested. For order  $N = 3$  polynomials, superconvergence for the coarsest grid is observed. The subconvergence behaviour observed on the grid with  $m = 16$  polynomials is most likely related to round-off errors of the variables with small magnitudes, meaning the discretisation errors are no longer dominant.

#### 4.3. The swinging motion of a pinned cable

In this part, the swinging motion of a cable in the air is evaluated. Several researchers addressed this problem numerically by comparing it against the available experimental data from Koh et al. (1999). However, in this test case, the numerical scheme results are compared with a simulation in the software Abaqus, which models the cable as a one-dimensional Timoshenko (shear flexible) beam (Lang et al., 2011; Martin and Bihs, 2021). This test case considers a cable in air with no sag, initially pinned at both ends between  $r_x = 0$  and  $r_x = L_0$ . One of the ends is released at time  $t = 0$ . Thus, the initial condition corresponds to

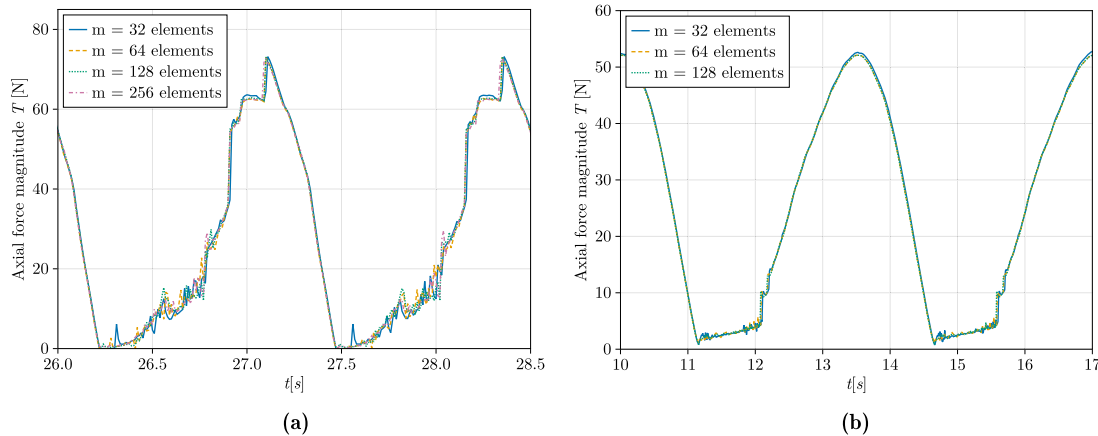


**Fig. 10.** Influence of the element size on the results of the test case with a) period  $\tau = 1.25$  s and b) period  $\tau = 3.50$  s and circular radius of  $R = 0.200$  m.

**Table 4**  
Numerical model parameters used, from Lang et al. (2011).

Length of cable, $L_0$ [m]	1.0
Mass of cable per unit length, $m_0$ [kg/m]	0.0864
Cable diameter, $d_0$ [m]	0.01
Cable density, $\rho_c$ [kg/m <sup>3</sup> ]	1100
Axial stiffness, $EA_0$ [N]	392.7
Bending stiffness, $EI$ [Nm <sup>2</sup> ]	0.0025

**Table 5**  
Numerical model parameters used to simulate the experimental setup of Bergdahl et al. (2016).

Length of line, $L_0$ [m]	33
Mass of line per unit meter, $m_0$ [kg/m]	0.0818
Equivalent line diameter, $d_0$ [m]	0.0022
Line density, $\rho_c$ [kg/m <sup>3</sup> ]	7800
Axial stiffness, $EA_0$ [N]	10000
Tangential drag coefficient, $C_{D_t}$ [-]	0.5
Normal drag coefficient, $C_{D_n}$ [-]	2.5
Tangential added mass coefficient, $C_{A_t}$ [-]	0
Normal added mass coefficient, $C_{A_n}$ [-]	3.8
Ground stiffness per unit meter, $k_{sb}$ [GPa/m]	3
Ground damping, $\beta_{sb}$ [-]	1
Ground friction coefficient, $\mu_{sb}$ [-]	0.3
Friction velocity, $v_f$ [-]	0.01

a straight cable, for which the material properties used in the numerical model are shown in [Table 4](#).

For the DG method, the cable is discretised by  $m = 16$  polynomials of order  $N = 4$ . The problem is simulated with a CFL = 0.05. The numerical results for the position and tension at different lengthwise cable positions are shown in [Fig. 5](#). Both numerical solutions display consistent behaviour, though subtle differences exist due to variations in cable modelling. The software *Abaqus* employs the Timoshenko beam model and discrete curvatures ([Lang et al., 2011](#)), while the current implementation uses the Euler-Bernoulli beam theory. Moreover, for the presented scheme, negative strain values in the solutions are not allowed, as visible in the plots. Despite these considerations, the overall results agree well.

#### 4.4. Catenary mooring chain in circular motion

This subsection validates the numerical model using experimental data for a dynamically excited catenary in a water tank ([Bergdahl et al., 2016](#)). The experimental setup schematics through which the numerical setup is based is shown in [Fig. 6](#).

This test case has been used in other works of the same scope ([Palm et al., 2017; Governo et al., 2023](#)). A brief overview of the test campaign is given below.

A catenary mooring chain of 33 m is placed in a 3 m deep water tank. On one end, the cable is fixed by a weight on the ground. The other end is connected to a rotating sheave installed slightly above the water level and spun at a defined rotational speed. At the same time, a load cell measures the tensile force. The tested rotational periods are  $\tau = 1.25$  s and  $\tau = 3.50$  s. A listing of the pertinent parameters concerning the experimental setup and utilised for the numerical model are presented in [Table 5](#), including the material characteristics of the mooring line. For the DG setup,  $m = 64$  polynomials of degree  $N = 4$  are used, with a CFL = 0.45. The boundary conditions are fixed position on the anchor side, and imposed motion (position and velocity) on the upper-end side.

In [Fig. 7](#), the tension magnitude time-series for a circular motion amplitude equal to 0.2m and both rotational periods is presented, comparing the numerical and experimental results. These timeseries represent experimental and numerical values after the initial transient period. For  $\tau = 1.25$ s ([Fig. 7a](#)), the numerical model shows strong consistency with the experimental data, particularly in reproducing the maximum tension values within the time series. The overall agreement between the model and measurements is also robust during the peak tension cycle. The tension behavior is actually a snap load propagation and reflection, as shown in [Governo et al. \(2023\)](#), [Palm et al. \(2017\)](#). In contrast, when the line tension approaches zero (the slackening regime), the numerical results exhibit pronounced fluctuations. Although similar oscillations are also present in the experimental data, their amplitude is smaller, suggesting that the numerical model tends to exaggerate this effect and introduce additional numerical noise. Moreover, the tension values are larger in this region, suggesting the seabed interaction model has a pronounced effect in the snap load mechanism in slack conditions, with local tension peaks in the nodal points ([Governo et al., 2023](#)). On the other hand, the results for  $\tau = 3.50$  s exhibited in [Fig. 7b](#)) are also in excellent agreement for the minimum and maximum tension values.

##### 4.4.1. Effect of the blending coefficient

To demonstrate the actuation of the blending coefficient  $\alpha$  in high-gradient/shock cases, the most dynamic condition of this experimental test, i.e.,  $R = 0.200$  m and  $\tau = 1.25$  s, is utilized. During the periodic motion, the line becomes slack with a null tension, and a steep tension gradient is formed and propagated along the line from the upper-end movement at  $s = L_0$ . This dynamic process is shown and compared in [Fig. 8](#), for a pure DG scheme (left) and the blended DG-FV scheme (right), with a range value  $0.01 < \alpha < 0.5$ . After the line slackens, tension increases from the upper end, creating a sharp gradient which activates

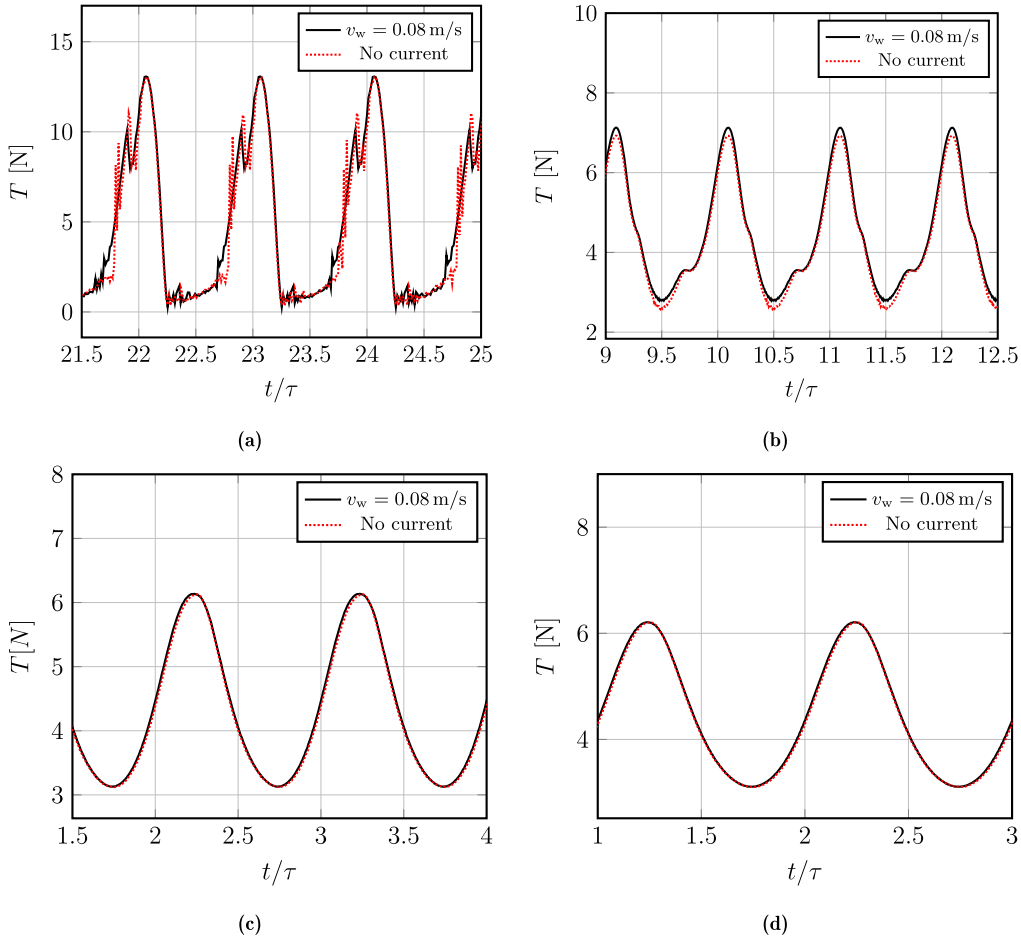


**Fig. 11.** Numerical time-series of the DG model in the experimental conditions of Barrera et al. (2019), for motion radius in surge  $R = 0.075 \text{ m}$  at periods of (a)  $\tau = 0.79 \text{ s}$ , (b)  $\tau = 1.58 \text{ s}$ , (c)  $\tau = 4.74 \text{ s}$  and (d)  $\tau = 6.32 \text{ s}$ .

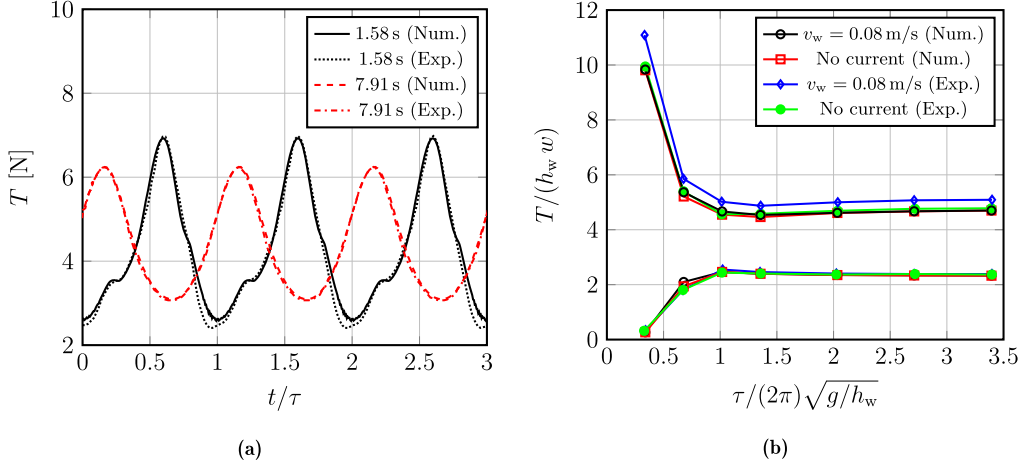


**Fig. 12.** Comparison of numerical results against the experimental data from Barrera et al. (2019): a) Time-series for different surge periods and  $R = 0.075 \text{ m}$  and b) non-dimensional maximum (top values) and minimum (bottom values) tension and for different non-dimensional periods, with and without current velocity.  $h_w$  is the water depth and  $w$  is the submerged weight per unit length.

the indicator function and follows the developing shock. The low-order scheme's dissipation reduces oscillations at the discontinuity. This velocity of the shock also depends on the dissipation of the scheme and causes slight alterations in the shape of the tension cycle at the fairlead, as plotted in Fig. 9. The blended scheme is seen to reduce oscillations during the low-tension cycle while reaching a slightly higher peak tension compared to the pure DG case.

#### 4.4.2. Grid sensitivity analysis

Here, a grid sensitivity study is conducted ensuring the solution is sufficiently accurate for the chosen element size. The polynomial order of  $N = 4$  is fixed and several grid spacings are used, with a constant refinement ratio of 2. The results are shown in Fig. 10.

The data indicates that the solution remains stable and shows minimal deviation with further refinement beyond  $m = 64$  polynomials.

**Table 6**

Numerical model parameters used to simulate the experimental setup of Barrera et al. (2019).

Length of line, $L_0$ [m]	7.305
Mass of line per unit meter, $m_0$ [kg/m]	0.115
Equivalent line diameter, $d_0$ [m]	0.0045
Line density, $\rho_c$ [kg/m <sup>3</sup> ]	7850
Axial stiffness, $E A_0$ [N]	20700
Tangential drag coefficient, $C_{D_t}$ [-]	1.44
Normal drag coefficient, $C_{D_n}$ [-]	0.66
Tangential added mass coefficient, $C_{A_t}$ [-]	0
Normal added mass coefficient, $C_{A_n}$ [-]	1.0
Ground stiffness per unit meter, $k_{sb}$ [MPa/m]	3
Ground damping, $\beta_{sb}$ [-]	1
Ground friction coefficient, $\mu_{sb}$ [-]	0.3
Friction velocity, $v_\mu$ [-]	0.01

Moreover, the calculated percentage errors in the maximum tension, relative to the most refined case, are 0.06% and 0.36% for the period  $\tau = 3.50\text{s}$  and 0.057%, 0.71% and 0.37% for the period  $\tau = 1.25\text{s}$ , listed in decreasing order of refinement. Overall, the most dynamic case shows greater sensitivity to variations in numerical parameters, as confirmed in this study. For the case of  $\tau = 3.50\text{s}$ , a less refined grid can be used.

#### 4.5. Catenary mooring chain in surge motion, with constant water current velocity

Data from Barrera et al. (2019) is used as the final test case for a laboratory catenary mooring chain. Their study conducted 1:40 model-scale tests under Froude similarity conditions of three chain diameters in a catenary configuration at the COCoTsU wave flume of the Environmental Hydraulics Institute of Cantabria (IH Cantabria). For a schematic of the experimental setup that served as the basis for the numerical setup, see Fig. 3 in Barrera et al. (2019). Several operating conditions were tested, but the present focus is on the two-dimensional surge movements under different amplitudes, radii, and periods. Moreover, the influence of the current velocity in the mooring line tensions is assessed. The numerical parameters used in the mooring model are tabulated in Table 6.

For the DG setup,  $m = 32$  polynomials of degree  $N = 4$  are used, with a CFL = 0.45. The boundary conditions are fixed position on the anchor side, and imposed motion (position and velocity) on the upper-end side. Several time-series comparisons are presented in Fig. 11, for  $R = 0.075\text{m}$  and different periods, and at different time windows. The periods used are  $\tau = 0.79, 1.58, 4.74$ , and  $6.32\text{s}$ . Moreover, the current velocity is  $v_w = 0.08\text{ m/s}$ . Note that the impact of the current velocity varies and depends on the oscillation frequency. At higher frequencies (smaller periods) of surge motion, the impact is more noticeable, where it is seen to change the tension cycle behaviour, Fig. 11a), or even decrease the maximum and minimum tensile force values, Fig. 11b). Contrarily, for larger periods, the impact is not evident, and there is almost no change in the tension behaviour in Fig. 11c) and d). However, a minor shift of the tension curve is verified.

Fig. 12 shows the non-dimensional plot containing the minimum and maximum values of the tension magnitude, with and without current velocity. Experimentally, it is evident that, for this test case, under these conditions, the impact of the current velocity is negligible for the minimum tension while it noticeably increases the maximum tension for all the periods tested consistently. The same is observed between numerical and experimental values, although in a less impactful way, with the numerical model underpredicting the maximum tension levels for the cases with current velocity. The reason for the difference is difficult to pinpoint. For instance, the results depend mainly on the hydrodynamic coefficients used (which rely on the Reynolds number) and on the experimental setup.

## 5. Conclusions

The accurate simulation of mooring line dynamics requires resolving transient loads such as snap loads with high fidelity, which are inadequately dissipated by the traditional low-order methods (lumped-mass and continuous finite-element approaches). This paper presents a high-order nodal discontinuous Galerkin method, enhanced with a sub-cell finite-volume formulation for shock capturing, to simulate the nonlinear dynamics of submerged mooring lines. The shock capturing is based on a blending formulation that requires the calculation of a shock indicator function. The model includes drag, hydrodynamics, elasticity, seabed interaction, bending and torsion. The bending and torsion formulation is based on a quasi-static angular momentum conservation that includes high-order strain gradients. These capabilities enable simulation of a wider range of cable types, including synthetic lines and power cables.

The results obtained with this method have been compared with analytical models and numerical and experimental data. The error analysis of a polynomial solution shows the optimal convergence rate of the scheme,  $N + 1$ . The numerical and experimental results shows a very good agreement, also including slack regimes. They also emphasized the sensitivity of the scheme to the numerical parameters of the model, particularly the sea bottom force under slack conditions. Under more regular conditions, the scheme demonstrated excellent convergence properties and high accuracy in most cases. Further research is needed to thoroughly assess the impact of the numerical parameters on the results.

## CRediT authorship contribution statement

**A.F.L. Governo:** Writing – original draft, Methodology, Investigation, Formal analysis, Data curation, Conceptualization; **J.C.C. Henriques:** Writing – review & editing, Supervision, Methodology, Funding acquisition, Conceptualization; **L.M.C. Gato:** Writing – review & editing, Supervision, Resources.

## Declaration of competing interest

The authors declare that they have no known competing financial interests or personal relationships that could have appeared to influence the work reported in this paper. The authors declare the following financial interests/personal relationships which may be considered as potential competing interests.

## Acknowledgements

The authors acknowledge Fundação para a Ciência e a Tecnologia (FCT) for its financial support via LAETA (project UID/50022/2025). The first author was supported by FCT grant no. DFA/BD/07315/2021.

## References

- Aamo, O.M., Fossen, T.I., 2000. Finite element modelling of mooring lines. *Math. Comput. Simul.* 53 (4–6), 415–422. [https://doi.org/10.1016/S0378-4754\(00\)00235-4](https://doi.org/10.1016/S0378-4754(00)00235-4)
- Aamo, O.M., Fossen, T.I., 2001. Finite Element Modelling of Moored Vessels. *Math. Comput. Model. Dyn. Syst.* 7 (1), 47–75. <https://doi.org/10.1076/mcmd.7.1.47.3632>
- Ablow, C.M., Schechter, S., 1983. Numerical simulation of undersea cable dynamics. *Ocean Eng.* 10 (6), 443–457. [https://doi.org/10.1016/0029-8018\(83\)90046-X](https://doi.org/10.1016/0029-8018(83)90046-X)
- Arnold, D.N., Brezzi, F., Cockburn, B., Marini, L.D., et al., 2002. Unified Analysis of Discontinuous Galerkin Methods for Elliptic Problems. *SIAM J. Numer. Anal.* 39 (5), 1749–1779. <https://doi.org/10.1137/S0036142901384162>
- Azconia, J., Munduate, X., González, L., Nyagaard, T.A., et al., 2017. Experimental validation of a dynamic mooring lines code with tension and motion measurements of a submerged chain. *Ocean Eng.* 129, 415–427. <https://doi.org/10.1016/j.oceaneng.2016.10.051>
- Barrera, C., Guanche, R., Losada, I.J., et al., 2019. Experimental modelling of mooring systems for floating marine energy concepts. *Mar. Struct.* 63, 153–180. <https://doi.org/10.1016/j.marstruc.2018.08.003>
- Bassi, F., Rebay, S., 1997. A High-Order Accurate Discontinuous Finite Element Method for the Numerical Solution of the Compressible Navier–Stokes Equations. *J. Comput. Phys.* 131 (2), 267–279. <https://doi.org/10.1006/jcph.1996.5572>

- Bergdahl, L., Palm, J., Eskilsson, C., Lindahl, J., et al., 2016. Dynamically scaled model experiment of a mooring cable. *J. Mar. Sci. Eng.* 4 (1), 5. <https://doi.org/10.3390/jmse4010005>
- Brown, D.T., Mavrakos, S., 1999. Comparative study on mooring line dynamic loading. *Mar. Struct.* 12 (3), 131–151. [https://doi.org/10.1016/S0951-8339\(99\)00011-8](https://doi.org/10.1016/S0951-8339(99)00011-8)
- Buckham, B., Driscoll, F.R., Nahon, M., et al., 2004. Development of a Finite Element Cable Model for Use in Low-Tension Dynamics Simulation. *J. Appl. Mech.* 71 (4), 476–485. <https://doi.org/10.1115/1.1755691>
- Canuto, C. (Ed.), 2006. *Spectral Methods: Fundamentals in Single Domains*. Scientific Computation, Springer, Berlin Heidelberg New York.
- Carpenter, M.H., Gottlieb, D., 1996. Spectral Methods on Arbitrary Grids. *J. Comput. Phys.* 129 (1), 74–86. <https://doi.org/10.1006/jcph.1996.0234>
- Chakrabarti, S.K., 2005. *Handbook of Offshore Engineering: Volume 1*. Elsevier, Amsterdam Oxford.
- Courant, R., Friedrichs, K., Lewy, H., 1928. Über die partiellen differenzengleichungen der mathematischen physik. *Math. Ann.* 100 (1), 32–74. <https://doi.org/10.1007/BF01448839>
- Cristescu, N., 2007. *Dynamic Plasticity*. World Scientific, Singapore ; Hackensack, NJ.
- Davidson, J., Ringwood, J., 2017. Mathematical modelling of mooring systems for wave energy converters - A review. *Energies* 10 (5), 666. <https://doi.org/10.3390/en10050666>
- DNV-GL, 2018. Position Mooring: DNV-GL Offshore Standard DNVGL-OS-E301. Technical Report.
- Faltinsen, O.M., 1999. *Sea Loads on Ships and Offshore Structures*. Cambridge Ocean Technology Series, Cambridge University Press, Cambridge. 1st Edition
- Fisher, T.C., Carpenter, M.H., 2013. High-order entropy stable finite difference schemes for nonlinear conservation laws: Finite domains. *J. Comput. Phys.* 252, 518–557. <https://doi.org/10.1016/j.jcp.2013.06.014>
- Fisher, T.C., Carpenter, M.H., Nordström, J., Yamaeev, N.K., Swanson, C., et al., 2013. Discretely conservative finite-difference formulations for nonlinear conservation laws in split form: Theory and boundary conditions. *J. Comput. Phys.* 234, 353–375. <https://doi.org/10.1016/j.jcp.2012.09.026>
- Garrett, D.L., 1982. Dynamic Analysis of Slender Rods. *J. Energy Resour. Technol.* 104 (4), 302–306. <https://doi.org/10.1115/1.3230419>
- Gassner, G., Kopriva, D.A., 2011. A Comparison of the Dispersion and Dissipation Errors of Gauss and Gauss-Lobatto Discontinuous Galerkin Spectral Element Methods. *SIAM J. Sci. Comput.* 33 (5), 2560–2579. <https://doi.org/10.1137/100807211>
- Gassner, G.J., Winters, A.R., Kopriva, D.A., et al., 2016. Split form nodal discontinuous Galerkin schemes with summation-by-parts property for the compressible Euler equations. *J. Comput. Phys.* 327, 39–66. <https://doi.org/10.1016/j.jcp.2016.09.013>
- Gobat, J.I., 2000. The Dynamics of Geometrically Compliant Mooring Systems. Doctor of Philosophy Massachusetts Institute of Technology and Woods Hole Oceanographic Institution. Woods Hole, MA. 1912/2720. <https://doi.org/10.1575/1912/2720>
- Gobat, J.I., Grosenbaugh, M.A., 2001. Application of the generalized-a method to the time integration of the cable dynamics equations. *Comput. Methods Appl. Mech. Eng.*, 13.
- Governo, A.F.L., Henriquez, J.C.C., Gato, L.M.C., et al., 2023. Modelling mooring line snap loads using a high-order finite-volume approach. *Ocean Eng.* 275, 113803. <https://doi.org/10.1016/j.oceaneng.2023.113803>
- Greiner, W., 2010. Classical Mechanics. Springer Berlin Heidelberg, Berlin, Heidelberg. <https://doi.org/10.1007/978-3-642-03434-3>
- Hall, M., Buckham, B., Crawford, C., et al., 2014. Evaluating the importance of mooring line model fidelity in floating offshore wind turbine simulations: mooring line model fidelity in floating wind turbine simulations. *Wind Energy* 17 (12), 1835–1853. <https://doi.org/10.1002/we.1669>
- Hennemann, S., Rueda-Ramírez, A.M., Hindenlang, F.J., Gassner, G.J., et al., 2021. A provably entropy stable subcell shock capturing approach for high order split form DG for the compressible Euler equations. *J. Comput. Phys.* 426, 109935. <https://doi.org/10.1016/j.jcp.2020.109935>
- Hesthaven, J.S., Warburton, T., 2008. *Nodal Discontinuous Galerkin Methods*. Vol. 54 of Texts in Applied Mathematics. Springer New York, New York, NY. <https://doi.org/10.1007/978-0-387-72067-8>
- Howell, C.T., 1992. *Investigation of the Dynamics of Low-Tension Cables*. Doctor of Philosophy. Massachusetts Institute of Technology. Department of Ocean Engineering.
- Karniadakis, G., Sherwin, S.J., 2005. *Spectral/Hp Element Methods for Computational Fluid Dynamics*. Oxford University Press, Oxford. 2nd Edition.
- Klöckner, A., Warburton, T., Hesthaven, J.S., 2011. Viscous Shock Capturing in a Time-Explicit Discontinuous Galerkin Method. *Math. Model. Nat. Phenom.* 6 (3), 57–83. <https://doi.org/https://doi.org/10.1051/m2npn/20116303>
- Koh, C.G., Zhang, Y., Quek, S.T., et al., 1999. Low-Tension Cable Dynamics: Numerical and Experimental Studies. *J. Eng. Mech.* 125 (3), 347–354. [https://doi.org/10.1061/\(ASCE\)0733-9399\(1999\)125:3\(347\)](https://doi.org/10.1061/(ASCE)0733-9399(1999)125:3(347))
- Kopriva, D.A., 2009. *Implementing Spectral Methods for Partial Differential Equations: Algorithms for Scientists and Engineers*. Scientific Computation, Springer Netherlands, Dordrecht. <https://doi.org/10.1007/978-90-481-2261-5>
- Kopriva, D.A., Gassner, G., 2010. On the Quadrature and Weak Form Choices in Collocation Type Discontinuous Galerkin Spectral Element Methods. *J. Sci. Comput.* 44 (2), 136–155. <https://doi.org/10.1007/s10915-010-9372-3>
- Landau, L.D., Lifshitz, E.M., 1975. *Course of Theoretical Physics: Theory of Elasticity. Vol. 7*.
- Lang, H., Linn, J., Arnold, M., et al., 2011. Multi-body dynamics simulation of geometrically exact Cosserat rods. *Multibody Syst. Dyn.* 25 (3), 285–312. <https://doi.org/10.1007/s11044-010-9223-x>
- LeVeque, R.J., 2002. *Finite Volume Methods for Hyperbolic Problems*. Cambridge University Press. 1st Edition. <https://doi.org/10.1017/CBO9780511791253>
- Markert, J., Gassner, G., Walch, S., et al., 2023. A sub-element adaptive shock capturing approach for discontinuous Galerkin methods. *Commun. Appl. Math. Computat.* 5 (2), 679–721. <https://doi.org/10.1007/s42967-021-00120-x>
- Martin, T., Bihs, H., 2021. A Numerical Solution for Modelling Mooring Dynamics, Including Bending and Shearing Effects, Using a Geometrically Exact Beam Model. *J. Mar. Sci. Eng.* 9 (5), 486. <https://doi.org/10.3390/jmse9050486>
- Masciola, M., Jonkman, J., Robertson, A., et al., 2012. Implementation of a Multisegmented, Quasi-Static Cable Model.
- Masciola, M., Robertson, A., Jonkman, J., Coulling, A., Goupee, A., et al., 2013. Assessment of the Importance of Mooring Dynamics on the Global Response of the DeepCwind Floating Semisubmersible Offshore Wind Turbine. p. 10.
- Montano, A., Restelli, M., Sacco, R., et al., 2007. Numerical simulation of tethered buoy dynamics using mixed finite elements. *Comput. Methods Appl. Mech. Eng.* 196 (41–44), 4117–4129. <https://doi.org/10.1016/j.cma.2007.04.012>
- Nava, V., Rajic, M., Guedes Soares, C., 2013. Effects of the mooring line configuration on the dynamics of a point absorber. In: Vol. 8: Ocean Renewable Energy. American Society of Mechanical Engineers, Nantes, France, V008T09A071. <https://doi.org/10.1115/OMAE2013-11141>
- Nordgren, R.P., 1974. On Computation of the Motion of Elastic Rods. *J. Appl. Mech.* 41 (3), 777–780. <https://doi.org/10.1115/1.3423387>
- Palm, J., Eskilsson, C., 2020. Influence of Bending Stiffness on Snap Loads in Marine Cables: A Study Using a High-Order Discontinuous Galerkin Method. *J. Mar. Sci. Eng.* 8 (10), 795. <https://doi.org/10.3390/jmse8100795>
- Palm, J., Eskilsson, C., Bergdahl, L., et al., 2017. An hp-adaptive discontinuous Galerkin method for modelling snap loads in mooring cables. *Ocean Eng.* 144, 266–276. <https://doi.org/10.1016/j.oceaneng.2017.08.041>
- Pecher, A., Kofoed, J.P. (Eds.), 2017. *Handbook of Ocean Wave Energy*. Vol. 7 of Ocean Engineering & Oceanography. Springer International Publishing, Cham. <https://doi.org/10.1007/978-3-319-39889-1>
- Persson, P.-O., Peraire, J., 2006. Sub-Cell Shock Capturing for Discontinuous Galerkin Methods. In: 44th AIAA Aerospace Sciences Meeting and Exhibit. American Institute of Aeronautics and Astronautics, Reno, Nevada. <https://doi.org/10.2514/6.2006-112>
- Petrone, C., Oliveto, N.D., Sivaselvan, M.V., et al., 2016. Dynamic Analysis of Mooring Cables with Application to Floating Offshore Wind Turbines. *J. Eng. Mech.* 142 (3), 04015101. [https://doi.org/10.1061/\(ASCE\)EM.1943-7889.0000999](https://doi.org/10.1061/(ASCE)EM.1943-7889.0000999)
- Polacheck, H., Walton, T.S., Mejia, R., Dawson, C., et al., 1963. Transient motion of an elastic cable immersed in a fluid. *Math. Comput.* 17 (81), 60–63. <https://doi.org/10.1090/S0025-5718-63-99187-7>
- Potluri, V.D., Puranik, B.P., Bodhi, K. V.R., 2023. High order discontinuous Galerkin simulation of hypersonic shock-boundary layer interaction using subcell limiting approach. *J. Comput. Phys.* 485, 112117. <https://doi.org/10.1016/j.jcp.2023.112117>
- Qiao, D., Haider, R., Yan, J., Ning, D., Li, B., et al., 2020. Review of wave energy converter and design of mooring system. *Sustainability* 12 (19), 8251. <https://doi.org/10.3390/su12198251>
- Quan, W., Chang, Q., Zhang, Q., Gong, J., 2020. Dynamics calculation for variable-length underwater cable with geometrically nonlinear motion. *Ocean Eng.* 212, 107695. <https://doi.org/10.1016/j.oceaneng.2020.107695>
- Rao, S.S., 2011. *Mechanical Vibrations*. Prentice Hall, Upper Saddle River, N.J. 5th Edition.
- Reed, W.H., Hill, T.R., 1973. Triangular mesh methods for the neutron transport equation. In: National Topical Meeting on Mathematical Models and Computational Techniques for Analysis of Nuclear Systems. United States.
- Rueda-Ramírez, A.M., Hennemann, S., Hindenlang, F.J., Winters, A.R., Gassner, G.J., et al., 2021. An entropy stable nodal discontinuous Galerkin method for the resistive MHD equations. Part II: Subcell finite volume shock capturing. *J. Comput. Phys.* 444, 110580. <https://doi.org/10.1016/j.jcp.2021.110580>
- Rui, S., Jostad, H.P., Zhou, Z., Bachynski-Polić, E., Sævik, S., Wang, L., Guo, Z., et al., 2025. Analysis of mooring system for floating wind turbine based on macro-model of chain-seabed interaction. *Mar. Struct.* 104, 103877. <https://doi.org/10.1016/j.marstruc.2025.103877>
- Rui, S., Zhou, Z., Gao, Z., Jostad, H.P., Wang, L., Xu, H., Guo, Z., et al., 2024. A review on mooring lines and anchors of floating marine structures. *Renewable Sustainable Energy Rev.* 199, 114547. <https://doi.org/10.1016/j.rser.2024.114547>
- Rui, S., Zhou, Z., Jostad, H.P., Wang, L., Guo, Z., et al., 2023. Numerical prediction of potential 3-dimensional seabed trench profiles considering complex motions of mooring line. *Appl. Ocean Res.* 139, 103704. <https://doi.org/10.1016/j.apor.2023.103704>
- Shu, C.-W., Osher, S., 1988. Efficient implementation of essentially non-oscillatory shock-capturing schemes. *J. Comput. Phys.* 77 (2), 439–471. [https://doi.org/10.1016/0021-9991\(88\)90177-5](https://doi.org/10.1016/0021-9991(88)90177-5)
- Tjavaras, A.A., 1996. *The Dynamics of Highly Extensible Cables*. Doctor of Philosophy. Massachusetts Institute of Technology. Department of Ocean Engineering. 1721.1/10730.
- Triantafyllou, M.S., Howell, C.T., 1994. Dynamic Response of Cables Under Negative Tension: an Ill-Posed Problem. *J. Sound Vib.* 173 (4), 433–447. <https://doi.org/10.1006/jsvi.1994.1239>
- Walton, T.S., Polacheck, H., 1960. Calculation of transient motion of submerged cables. *Math. Comput.* 14, 27–46.
- Wang, L., Rui, S., Guo, Z., Gao, Y., Zhou, W., Liu, Z., et al., 2020. Seabed trenching near the mooring anchor: History cases and numerical studies. *Ocean Eng.* 218, 108233. <https://doi.org/10.1016/j.oceaneng.2020.108233>
- Xiong, L., Yang, J., Zhao, W., et al., 2016. Dynamics of a taut mooring line accounting for the embedded anchor chains. *Ocean Eng.* 121, 403–413. <https://doi.org/10.1016/j.oceaneng.2016.05.011>